

# Photodynamical modeling of TOI-4504 reveals its deeply resonant state and similarity to GJ 876

J.M. Almenara<sup>1</sup>, R. Mardling<sup>2,1</sup>, A. Leleu<sup>1</sup>, S. Udry<sup>1</sup>, T. Forveille<sup>3</sup>, X. Bonfils<sup>3</sup>, F. Bouchy<sup>1</sup>,  
C. Cadieux<sup>1</sup>, J. Couturier<sup>1</sup>, R.F. Díaz<sup>4,5</sup>, Y. Eyholzer<sup>1</sup>, E. Fontanet<sup>1</sup>, T. Guillot<sup>6</sup>, G. Hébrard<sup>7,8</sup>,  
R.M. Hoogenboom<sup>1</sup>, J. Korth<sup>1</sup>, M. Lendl<sup>1</sup>, and A. Nigioni<sup>1</sup>

<sup>1</sup> Observatoire de Genève, Département d’Astronomie, Université de Genève, Chemin Pegasi 51b, 1290 Versoix, Switzerland

<sup>2</sup> School of Physics and Astronomy, Monash University, Victoria, 3800, Australia

<sup>3</sup> Univ. Grenoble Alpes, CNRS, IPAG, F-38000 Grenoble, France

<sup>4</sup> Instituto Tecnológico de Buenos Aires (ITBA), Iguazú 341, Buenos Aires, CABA C1437, Argentina

<sup>5</sup> Instituto de Ciencias Físicas (ICIFI; CONICET), ECyT-UNSAM, Campus Miguelete, 25 de Mayo y Francia, (1650) Buenos Aires, Argentina

<sup>6</sup> Université Côte d’Azur, Laboratoire Lagrange, OCA, CNRS UMR 7293, Nice, France

<sup>7</sup> Institut d’astrophysique de Paris, UMR7095 CNRS, Université Pierre & Marie Curie, 98bis boulevard Arago, 75014 Paris, France

<sup>8</sup> Observatoire de Haute-Provence, 04670 Saint Michel l’Observatoire, France

## ABSTRACT

The K-dwarf TOI-4504 hosts two giant planets in 2:1 mean-motion resonance, with orbital periods of 41.3 days (planet d) and 82.8 days (planet c). They exhibit among the largest known absolute transit-timing variations, with respective peak-to-node amplitudes up to 5 and 3 days. Newer TESS data show that the previously non-transiting planet d has now precessed into transiting, and we derive updated system parameters with significant discrepancies with the discovery paper. The revised parameters place planets d and c deep in the resonance and close to or in the fully-relaxed limit-cycle state, with the resonant and secular modes interfering nonlinearly to induce non-zero relaxed free eccentricities which precess at the same rate as the forced eccentricities and the longitude of conjunctions, in turn enabling precise measurement of the full eccentricities and apsidal angles. We discuss the predictions of linear theory and how it can be used to understand the true state of the system revealed by  $N$ -body integrations, and more generally why it is that the posteriors of systems more compact than 2:1 tend to suffer from significant eccentricity degeneracy. We show that the extraordinary dynamical states of the giant pairs orbiting TOI-4504 and the M-dwarf GJ 876 are remarkably similar, in spite of the significant difference in their host-star masses, and discuss the implications for damping timescales during the relatively gentle formation process of Type II migration.

**Key words.** stars: individual: TOI-4504, GJ 876, TOI-216, TOI-1130, TOI-1408, TOI-7510, K2-19, K2-266, Kepler-9, Kepler-18, Kepler-36, Kepler-88 – stars: planetary systems – planets and satellites: dynamical evolution and stability – planets and satellites: formation – techniques: photometric – techniques: radial velocities

## 1. Introduction

Vítková et al. (2025) discovered the TOI-4504 system with the Transiting Exoplanet Survey Satellite (TESS; Ricker et al. 2015). They found that the K1V stellar host is transited by a sub-Neptune in a 2.4-days orbit (planet b) and by a Jupiter-sized planet with a period of 82.5 days (planet c). TOI-4504 c exhibited among the largest absolute transit-timing variations (TTVs; Agol et al. 2005; Holman & Murray 2005) known, with a peak-to-node amplitude of  $\sim 2$  days. The large TTVs indicate a strong dynamical interaction. Using radial-velocity (RV) measurements, Vítková et al. (2025) identified the perturber, TOI-4504 d, as a non-transiting inner giant planet in 2:1 mean-motion resonance (MMR) with planet c.

TESS obtained additional photometry of TOI-4504 in 2025, which covers three additional transits of TOI-4504 c and even more importantly reveals that the previously non-transiting planet d has precessed into a transiting configuration. These observations motivate our reanalysis of the system. We report significantly different system parameters compared to the discov-

ery paper, and investigate the dynamical implications of these updated parameters.

The article is organized as follows: We describe the observations of TOI-4504 in Sect. 2. Section 3 presents the analysis of the transit data and the literature RV measurements. Finally, we discuss our results in Sect. 4 which includes a comparison with the results of Vítková et al. (2025), as well as a detailed examination of the relaxed dynamical state of the giant pair in TOI-4504, its similarities with the giant pair in GJ 876, and the implications for Type-II migration. The formalism used to draw our conclusions is summarized in Appendix B which includes a list of systems in various related dynamical states.

## 2. Observations

TOI-4504 lies in the TESS southern continuous viewing zone, near the south ecliptic pole, and was observed in 43 sectors between 2018 and 2026. During Sectors 1-13, it was monitored only in full-frame images (FFIs), with a cadence of 1800 seconds. TOI-4504 was later upgraded to a 120 seconds cadence in Sectors 27-38, 61-65, 67-69, 87-90, and 94-98. When avail-

able, we used the presearch data-conditioning simple aperture photometry (PDCSAP; Smith et al. 2012, Stumpe et al. 2012, 2014) light curves of TOI-4504, produced by the TESS Science Processing Operations Center (SPOC; Jenkins et al. 2016; Caldwell et al. 2020), with the exception of the transit of planet c in Sector 61 which is only available in simple aperture photometry. For the observations in FFIs only, we produced light curves using *TESSCut* (Brasseur et al. 2019) from FFIs calibrated by SPOC, and performed photometry with the *Lightkurve* package (*Lightkurve Collaboration et al. 2018*)<sup>1</sup>. Prior to the availability of the light curve produced by SPOC for Sector 98, we made use of the TESS Image CALibrator Full Frame Images (TICA; Fausnaugh et al. 2020), which have a cadence of 200 seconds.

We analyzed a dataset consisting of 27-hour segments centered on the transits of planets c and d, corresponding to approximately three times the transit duration of planet c. For planet d, we also included the epochs of minimum star-planet projected separation in Sectors 62–69, even though no transits were detected, in order to exclude transiting configurations at these times. The shorter transits of planet b were incorporated only from sectors with 120-second cadence, using shorter segments of 7.5 hours around each transit.

In addition to the TESS data, we included ground-based observations of the egress of planet c on 12 January 2026 and the full transit of planet d on 22 January 2026, obtained with EulerCam (ECAM; Lendl et al. 2012) on the Swiss 1.2 m Euler telescope at La Silla Observatory. Observations were conducted with the NGTS filter, using exposure times ranging from 40 to 80 seconds. The image reduction was carried out following Lendl et al. (2012) and Lendl (2014). Aperture photometry was performed using *prose* (Garcia et al. 2022), which relies on *astropy* (Astropy Collaboration et al. 2022) and *photutils* (Bradley 2023). The optimal differential photometry followed Broeg et al. (2005). Alongside these photometric datasets, we also included the RV measurements obtained with the FEROS spectrograph (Kaufer et al. 1999) and reported by Vítková et al. (2025).

### 3. Analysis

We jointly fit the observed photometry and RVs using a photodynamical model (Carter et al. 2011) that accounts for the gravitational interactions among the four known bodies in the system. Their positions and velocities were computed as a function of time using the *N*-body code REBOUND (Rein & Liu 2012) employing the WHFast integrator (Rein & Tamayo 2015) with a time step of 0.02 days. The sky-projected positions were used to generate the light curve with *batman* (Kreidberg 2015), incorporating the light-time effect (Irwin 1952). Oversampling was applied to the TESS data to account for the integration-induced distortion described by Kipping (2010). The line-of-sight velocity of the star, derived from the *N*-body integration, was used to model the RV measurements. The model was parameterized using the stellar mass and radius, limb-darkening coefficients, planet-to-star mass and radius ratios, and Jacobi orbital elements (Table 1) at the reference epoch ( $t_{\text{ref}} = 2\,460\,886.2838 \text{ BJD}_{\text{TDB}}$ ). Due to the symmetry of the problem, we fixed the longitude of the ascending node of planet c at  $t_{\text{ref}}$  to  $180^\circ$ , and constrained the inclination of planet d to be less than  $90^\circ$ . For the ECAM observations, we included a linear model in the peak value of

<sup>1</sup> BJD<sub>TDB</sub> times for the target observations were computed following <https://github.com/havijw/tess-time-correction>.

the point-spread function and the airmass, and we modeled the error terms using Gaussian-process regression, adopting the approximate Matern kernel implemented in *celerite* (Foreman-Mackey et al. 2017). The model for the RV has two additional parameters: the systemic velocity and a jitter term. In total, the model comprises 41 free parameters. We adopted normal priors for the stellar mass and radius from Vítková et al. (2025), and uninformative priors for the remaining parameters. The joint posterior distribution was sampled using the *emcee* algorithm (Goodman & Weare 2010; Foreman-Mackey et al. 2013).

The maximum a posteriori (MAP) model for the transit photometry is plotted in Fig. 1. Table 1 lists the median and the 68% credible interval (CI) of the marginal distribution of the inferred system parameters. Figure 2 present the posterior TTVs for planets d and c, derived from the times of minimum projected separation between the star and planet, and a comparison with the individually determined transit times (Table 2) computed with *juliet* (Espinoza et al. 2019; Kreidberg 2015; Speagle 2020), assuming a constant transit duration. Figure 3 shows the transit duration for planets d and c, calculated from the difference of the first and fourth contact times, as obtained from the sky-projected star–planet separation. Figures 4 and 5 show, respectively, the posterior top-view planet orbits and the stellar-crossing path as seen by the observer, both derived from the MAP model.

Our model provides a poor fit to the FEROS RVs (Fig. 6), as did Vítková et al. (2025)’s. The posterior value of the FEROS multiplicative jitter is  $7.3 \pm 1.0$ , corresponding to approximately 86 m/s effective RV uncertainties. We detect no significant periodicity in the residuals that would indicate that the system contains an additional planet. Introducing into a fit of the RV data alone a planet between planets b and d, beyond c, or both, does not significantly reduce the jitter. The excess signal may therefore be at least partially attributable to stellar activity. Vítková et al. (2025) reported that several activity indicators (Bisector,  $H\alpha$ ,  $\text{He I}$ ,  $\text{Na II}$ ) show no significant periodicities, but the  $\log R'_{\text{HK}}$  index shows multiple marginally significant periods, indicating that TOI-4504 is an active star. The  $\log R'_{\text{HK}}$  index, with weighted mean and standard deviation of  $-4.43 \pm 0.38$ , reaches values as high as  $-3.92 \pm 0.05$ , which could imply RV scatter of tens to a few hundreds of m/s (Hojjatpanah et al. 2020). It is also possible that the FEROS uncertainties are underestimated. Finally, additional planets remain a possible explanation.

### 4. Results and discussion

The only dynamical constraint we can place on planet b is an upper mass limit of  $100 M_{\text{E}}$  at 95% confidence. In the following, we therefore concentrate on planets d and c, the Jupiter-size pair in the 2:1 MMR, for which we have achieved a more detailed characterization, provided that the model is correct. This would no longer hold if the system would contain additional dynamically relevant planets.

The measured masses ( $2.0$  and  $2.6 M_{\text{J}}$ ) and radii ( $\approx 1 R_{\text{J}}$ ) place both planets in the regime of compact, non-inflated warm Jupiters. Their equilibrium temperatures of 525 K and 413 K are too low for radius-inflation mechanisms to operate efficiently (Demory & Seager 2011). Consequently, their densities are consistent with standard cooling–contraction models (Guillot 2005; Fortney et al. 2007). The high surface gravities imply small atmospheric scale heights, and neither planet is an easy target for transmission spectroscopy. Nevertheless, their temperatures fall in an interesting regime for atmospheric chemistry, where cloud formation and the  $\text{CO}$ – $\text{CH}_4$  transition become important (Lodders & Fegley 2002), possibly allowing the possibility to

**Table 1.** Inferred system parameters.

Parameter	Units	Prior	Median and 68.3% CI		
<b>Star</b>					
Stellar mass, $m_\star$	( $M_\odot$ )	$N(0.89, 0.06)$	$0.877 \pm 0.055$		
Stellar radius, $R_\star$	( $R_\odot^N$ )	$N(0.92, 0.04)$	$0.931 \pm 0.026$		
Stellar mean density, $\rho_\star$	( $\text{g cm}^{-3}$ )		$1.53 \pm 0.11$		
Surface gravity, $\log g$	(cgs)		$4.442 \pm 0.025$		
$q_1$ TESS, ECAM		$U(0, 1)$	$0.30^{+0.25}_{-0.14}, 0.23^{+0.27}_{-0.14}$		
$q_2$ TESS, ECAM		$U(0, 1)$	$0.32^{+0.37}_{-0.21}, 0.22^{+0.35}_{-0.17}$		
<b>Planets</b>					
			<b>Planet b</b>	<b>Planet d</b>	<b>Planet c</b>
Semi-major axis, $a$	(au)		$0.03382 \pm 0.00072$	$0.2221 \pm 0.0047$	$0.3595 \pm 0.0076$
Eccentricity, $e$			$< 0.74^\dagger$	$0.2930 \pm 0.0012$	$0.04989 \pm 0.00023$
Argument of periastron, $\omega$	( $^\circ$ )		$180 \pm 160$	$195.97 \pm 0.15$	$178.51 \pm 0.54$
Inclination, $i$	( $^\circ$ )	$S(0, 180)_{b,c}, S(0, 90)_d$	$92.5^{+2.0}_{-4.2}$	$88.981 \pm 0.036$	$89.543 \pm 0.034$
Longitude of the ascending node, $\Omega$	( $^\circ$ )	$U(90, 270)_{b,d}$	$215 \pm 33$	$182.03 \pm 0.26$	$180$ (fixed at $t_{\text{ref}}$ )
Mean anomaly, $M_0$	( $^\circ$ )		$196^{+76}_{-41}$	$166.28 \pm 0.26$	$277.30 \pm 0.55$
$\sqrt{e} \cos \omega$		$U(-1, 1)$	$-0.15^{+0.79}_{-0.41}$	$-0.5205 \pm 0.0013$	$-0.22328 \pm 0.00049$
$\sqrt{e} \sin \omega$		$U(-1, 1)$	$-0.01 \pm 0.24$	$-0.1489 \pm 0.0012$	$0.0058 \pm 0.0021$
Mass ratio, $m_p/m_\star$		$U(0, 1)$	$< 35 \times 10^{-5}^\dagger$	$(220.49 \pm 0.69) \times 10^{-5}$	$(281.66 \pm 0.34) \times 10^{-5}$
Radius ratio, $R_p/R_\star$		$U(0, 1)$	$0.02603 \pm 0.00085$	$0.1103 \pm 0.0033$	$0.1102 \pm 0.0020$
Scaled semi-major axis, $a/R_\star$			$7.81 \pm 0.18$	$51.3 \pm 1.2$	$83.0 \pm 2.0$
Impact parameter, $b$			$0.37 \pm 0.25$	$0.906 \pm 0.013$	$0.659 \pm 0.036$
$T'_0 - 2\,460\,000$	(BJD <sub>TDB</sub> )	$U(-114, 1887)$	$887.1883 \pm 0.0030$	$900.0759 \pm 0.0017$	$886.2585 \pm 0.0016$
$P'$	(d)	$U(0, 1000)$	$2.42634 \pm 0.00014$	$40.8204 \pm 0.0024$	$84.0725 \pm 0.0049$
$K'$	( $\text{m s}^{-1}$ )		$< 57^\dagger$	$136.5 \pm 2.9$	$131.2 \pm 2.8$
Planet mass, $m_p$	( $M_E$ )		$< 100^\dagger$	$644 \pm 40$	$822 \pm 51$
	( $M_J$ )		$< 0.32^\dagger$	$2.03 \pm 0.13$	$2.59 \pm 0.16$
Planet radius, $R_p$	( $R_E^N$ )		$2.65 \pm 0.12$	$11.19 \pm 0.54$	$11.18 \pm 0.43$
	( $R_J^N$ )		$0.236 \pm 0.011$	$0.999 \pm 0.048$	$0.998 \pm 0.038$
Planet mean density, $\rho_p$	( $\text{g cm}^{-3}$ )		$< 31^\dagger$	$2.52 \pm 0.34$	$3.22 \pm 0.40$
Planet surface gravity, $\log g_p$	(cgs)		$3.81^{+0.23}_{-0.40}$	$3.702 \pm 0.042$	$3.808 \pm 0.037$
Equilibrium temperature, $T_{\text{eq}}$	(K)		$1345 \pm 22$	$525.0 \pm 8.6$	$412.6 \pm 6.8$
Mutual inclination, $I_{d,c}$	( $^\circ$ )			$2.11 \pm 0.25$	
<b>RV</b>					
FEROS jitter		$U(0, 20)$	$7.3 \pm 1.0$		
FEROS offset	( $\text{m s}^{-1}$ )	$U(-10^5, 10^5)$	$2070 \pm 14$		
<b>Linear ephemerides</b>					
Period	(d)		$2.4261518$	$41.2872390$	$82.8190895$
$T_0 - 2\,450\,000$	(BJD <sub>TDB</sub> )		$8395.529998$	$8423.049769$	$8400.937342$

**Notes.** The table lists: Prior, posterior median, and 68.3% credible interval (CI) for the photodynamical analysis (Sect. 3). The Jacobi orbital elements are given for the reference epoch  $t_{\text{ref}} = 2\,460\,886.2838$  BJD<sub>TDB</sub>. The parameters  $q_1$  and  $q_2$  are the quadratic limb-darkening coefficients parameterized using Kipping (2013).  $^\dagger$  Upper limit at 95% confidence. The planetary equilibrium temperature is computed for zero albedo and full day-night heat redistribution.  $P'$  and  $T'_0$  should not be confused with the linear ephemeris, and they were only used to reduce the correlations between jump parameters, replacing the semi-major axis and the mean anomaly at  $t_{\text{ref}}$ . The linear ephemerides are derived from the median posterior transit times spanning the years 2018 to 2027.

$T'_0 \equiv t_{\text{ref}} - \frac{P'}{2\pi} (M_0 - E + e \sin E)$  with  $E = 2 \arctan \left\{ \sqrt{\frac{1-e}{1+e}} \tan \left[ \frac{1}{2} (\frac{\pi}{2} - \omega) \right] \right\}$ ,  $P' \equiv \sqrt{\frac{4\pi^2 a^3}{G m_\star}}$ ,  $K' \equiv \frac{m_p \sin i}{m_\star^{2/3} \sqrt{1-e^2}} \left( \frac{2\pi G}{P'} \right)^{1/3}$ . CODATA 2018:  $G = 6.674\,30 \times 10^{-11} \text{ m}^3 \text{ kg}^{-1} \text{ s}^{-2}$ . IAU 2012:  $\text{au} = 149\,597\,870\,700 \text{ m}$ . IAU 2015:  $R_\odot^N = 6.957 \times 10^8 \text{ m}$ ,  $(GM)_\odot^N = 1.327\,124\,4 \times 10^{20} \text{ m}^3 \text{ s}^{-2}$ ,  $R_E^N = 6.378\,1 \times 10^6 \text{ m}$ ,  $(GM)_E^N = 3.986\,004 \times 10^{14} \text{ m}^3 \text{ s}^{-2}$ ,  $R_J^N = 7.149\,2 \times 10^7 \text{ m}$ ,  $(GM)_J^N = 1.266\,865\,3 \times 10^{17} \text{ m}^3 \text{ s}^{-2}$ .  $M_\odot = (GM)_\odot^N/G$ ,  $M_E = (GM)_E^N/G$ ,  $M_J = (GM)_J^N/G$ ,  $k^2 = (GM)_\odot^N (86\,400 \text{ s})^2 / \text{au}^3$ .  $N(\mu, \sigma)$ : Normal distribution with mean  $\mu$  and standard deviation  $\sigma$ .  $U(a, b)$ : A uniform distribution defined between a lower  $a$  and upper  $b$  limit.  $S(a, b)$ : A sinusoidal distribution defined between a lower  $a$  and upper  $b$  limit.

constrain the planets' internal luminosities (see Welbanks et al. 2024; Sing et al. 2024).

The TTVs (Figs. 2 and 7) show two main periodicities: the resonant period ( $P_R \sim 2.5$  years) and the superperiod ( $P_S \sim 33$  years; Lithwick et al. 2012). The origin of these two periods is discussed in Sect. 4.2. The peak-to-node TTV amplitudes on the timescale of the superperiod (Fig. 7) reach about 5.2 days for planet d and about 3.4 days for planet c (these values respectively correspond to 13% and 4.1% of the corresponding orbital periods), whereas the amplitudes over the time span of the observations are about 2 days for both planets. These are among the

largest absolute TTV amplitudes known (see Fig. 11 in McKee & Montet 2023 and Fig. 10 in Vítková et al. 2025). The transit forecast from the current modeling shows large uncertainties, reaching up to 28 minutes in 2026. Observing additional transits, which have timing precision of a few minutes, would therefore significantly improve the system parameters.

The orbital planes of planets d and c precess with a period of approximately 250 years. Together with their inclinations relative to the line of sight and the measured mutual inclination, this geometry causes planets d and c to intermittently cease transiting (see Fig. 8). Currently, both planets transit. According to

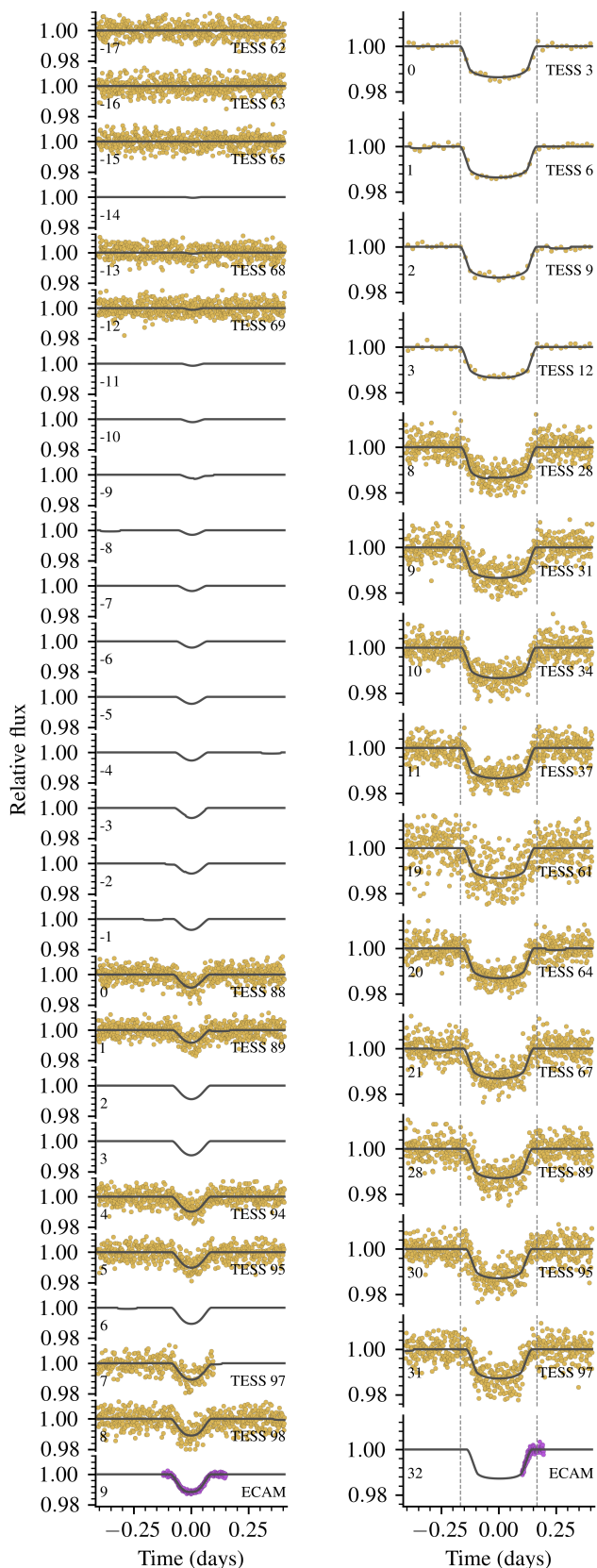


**Fig. 1.** Photodynamical modeling of the transits of planets d (left) and c (right). The dots represent the observations. The black line shows the oversampled transit model. Each panel is centered at the MAP transit timing and labeled with the epoch number and the sector for TESS observations. For planet c, the dashed vertical lines delimit a transit duration of 8 hours, close to the maximum value during the observations.

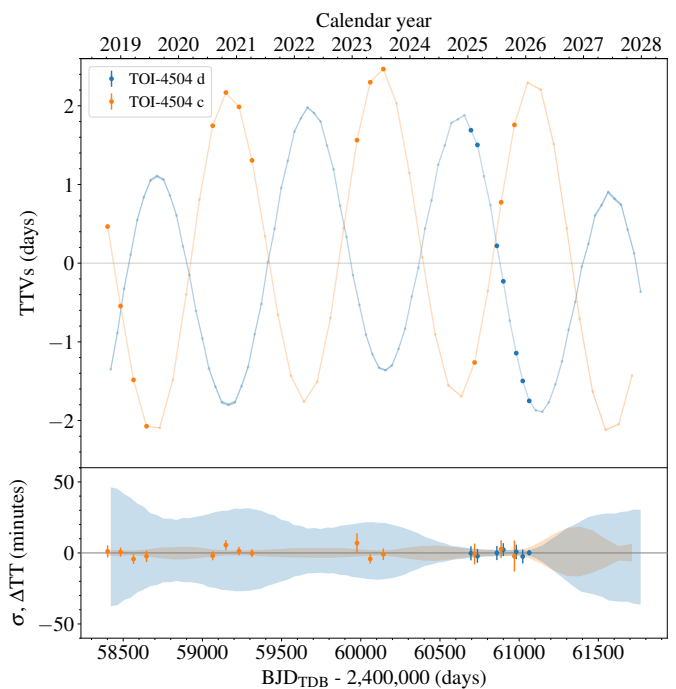


**Fig. 2.** Posterior TTV predictions of planets d (blue) and c (orange) computed relative to a linear ephemeris (Table 1). A thousand random draws from the posterior distribution were used to estimate the median TTV values and their uncertainties (68.3% confidence interval). The upper panel shows the posterior TTV values and compares them with the individual transit-time determinations (Table 2, error bars). In the lower panel, the posterior median transit-timing value was subtracted to emphasize the uncertainty in the distribution and facilitate a clearer comparison with the individually determined transit times.

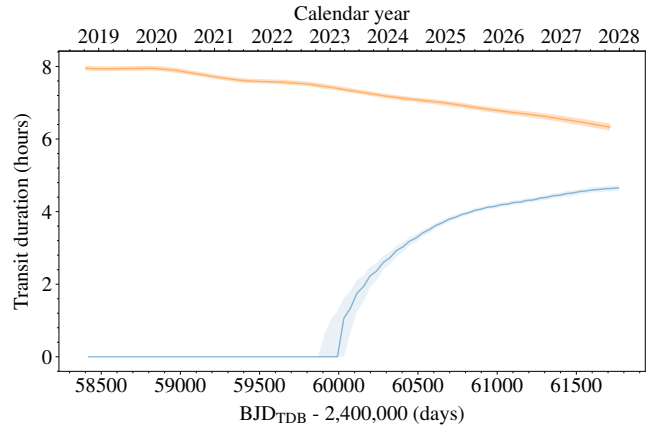


**Fig. 3.** Posterior of the transit duration of planets d (blue) and c (orange). We used a thousand random draws from the posterior distribution to estimate the median transit duration and its uncertainty (68.3% CI). A duration of zero correspond with the planet not transiting.

the model, planet d began transiting in late 2022 or early 2023 (although initially with such shallow grazing transit that they were not detectable by TESS) and will keep doing so for the next  $\sim 150$  years, whereas planet c is expected to stop transiting around 2042 for roughly the following  $\sim 130$  years. This behavior recurs on the 250-year precession cycle.

Photodynamical modeling of TOI-4504 provides significantly better constraints on the system parameters than an analysis based only on transit times (TTV analysis): both the planet-to-star mass ratios and the orbital eccentricities are determined

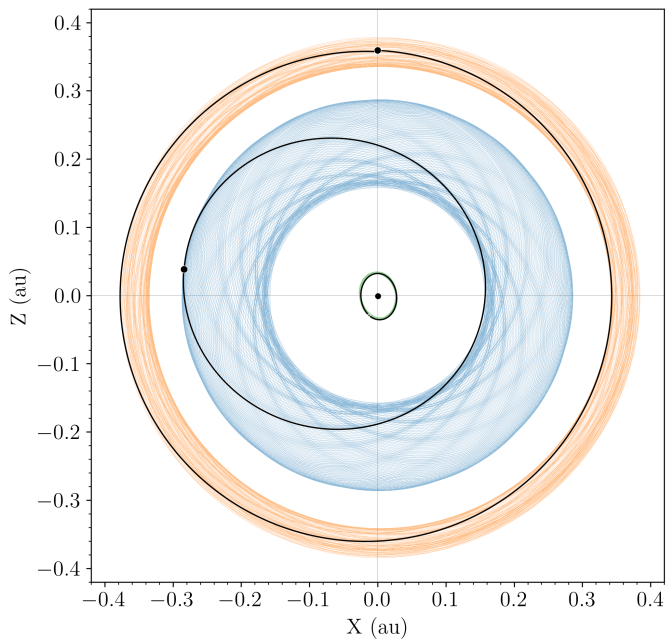


**Fig. 4.** Orbital projection of the MAP model over the time-span of the superperiod for planet b (green), d (blue), and c (orange). The origin is the system barycenter, and the orbits are projected in the X-Z plane (system top view, movement is clockwise, the positive Z-axis points towards the observer). One orbit near  $t_{\text{ref}}$  is shown in black. The black circles mark the position of the star (size to scale) and the planets (enlarged by a factor of 10) at  $t_{\text{ref}}$ .

with a precision better than 1%. Eccentricities and planet-to-star mass ratios are determined 52% to 58% more precisely with photodynamical modeling than with TTV analysis. In addition to the transits of planet d appearing and changing shape, the transit duration variations of planet c are visible by eye (Fig. 1); together these constrain the mutual inclination to  $2.11 \pm 0.25^\circ$ . A TTV analysis of planets d and c can, by contrast, only constrain their mutual inclination to  $< 6.2^\circ$  at 95% confidence level, and this value corresponds to a lower limit since the inclinations of both planets were fixed at  $90^\circ$  at  $t_{\text{ref}}$ .

#### 4.1. Comparison with Vítková et al. (2025)

Vítková et al. (2025) correctly identified the 2:1 perturber. However, their reported system parameters differ substantially from ours, with masses of  $1.42^{+0.07}_{-0.06} M_J$  and  $3.77 \pm 0.18 M_J$ , and eccentricities<sup>2</sup> of  $0.0445^{+0.0010}_{-0.0009}$  and  $0.0320^{+0.0016}_{-0.0014}$  for planets d and c, respectively. Their adopted priors for the parameter space exploration (Table A1 in Vítková et al. 2025) excluded the solution found in this work, specifically the mass (parameterized by the stellar RV amplitude) and eccentricity (parameterized as  $e \cos \omega$ ,  $e \sin \omega$ ) of planet d. To explore this further, we broadened their prior on orbital eccentricities and allowed for higher planet-to-star mass ratios, finding a multimodal posterior, including one mode compatible with the solution of Vítková et al. (2025) and another consistent with our own posterior (see Appendix A). This illustrates the degeneracies inherent in TTV inversions when the perturber is not observed in transit, which can

<sup>2</sup> The eccentricities are osculating values for different reference epochs, but orbital evolution only makes a minor contribution to the discrepancy.

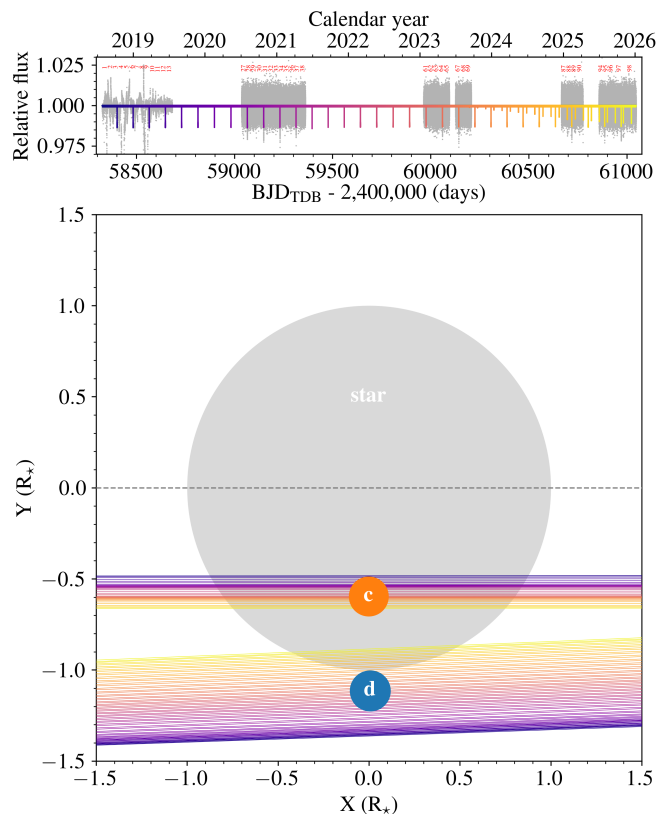


**Fig. 5.** Stellar-crossing paths of planets d and c as seen by the observer for the MAP model. The stellar disc is shown in gray, and the MAP planet radii are indicated by blue (planet d) and orange (planet c) disks. The upper panel displays the TESS light curve (gray dots) together with the MAP transit model, with the model color-coded by time. The same color scale is used in the main panel for the crossing paths. The TESS sector is annotated in red.

lead to significantly different system parameters all matching the transit times.

We note that the argument of periastron and the mean anomaly reported in Table 4 of Vítková et al. (2025) correspond to the stellar orbit (Householder & Weiss 2022), despite the caption stating that the orbital elements are given in the Jacobi frame. Consequently, to recover their published TTV fit, we added  $180^\circ$  to those angles before inputting the maximum-likelihood solution into their TTV code (TTVFast; Deck et al. 2014).

We also tested the maximum-likelihood solution of Vítková et al. (2025) using the resonance model outlined in Appendix B and found that it corresponds to a system in the non-resonant librating state with  $R = 1.4$ . In particular their average period ratio is 2.061 with associated superperiod 1352 days, while our average period ratio is 2.006, placing the system much deeper in the resonance with superperiod 33.4 years. Note that at around 930 days, the TTV signal varies with the resonant period, not the superperiod as stated by Vítková et al. (2025).

#### 4.2. Relaxed dynamical state and similarities with GJ 876

GJ 876 is a non-transiting 4-planet M-dwarf system for which the three outer planets (whose masses and periods are  $m_c = 0.9 M_J$ ,  $m_b = 2.6 M_J$  and  $m_e = 0.05 M_J$ , and  $P_c = 30.1$  d,  $P_b = 61.1$  d and  $P_e = 123.8$  d) participate in a 4:2:1 Laplace resonance (Delfosse et al. 1998; Marcy et al. 1998, 2001; Rivera

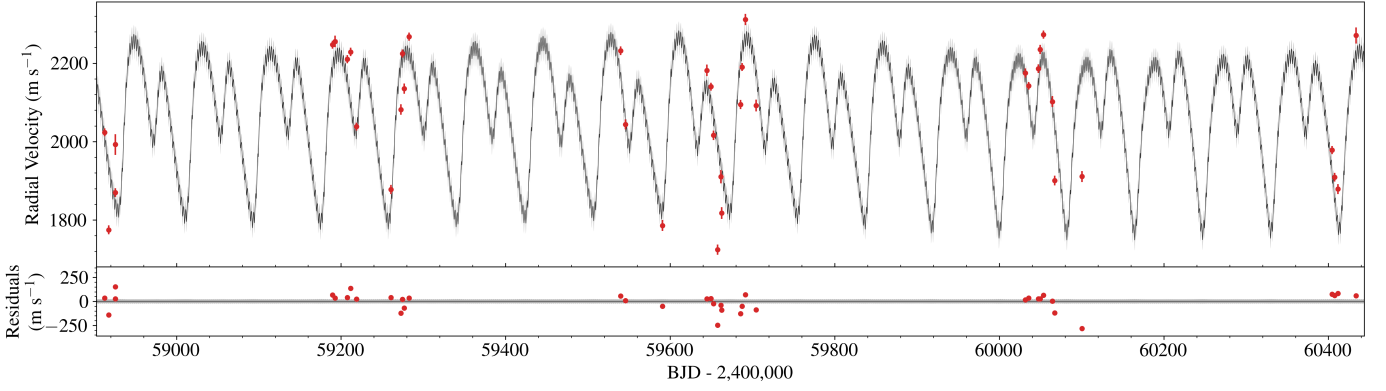


**Fig. 6.** FEROS RVs of TOI-4504 (red error bars) together with the median RV model (black line) and the 68.3% confidence interval (gray region), both estimated from a thousand random draws from the posterior distribution. Residuals from the median model are shown.

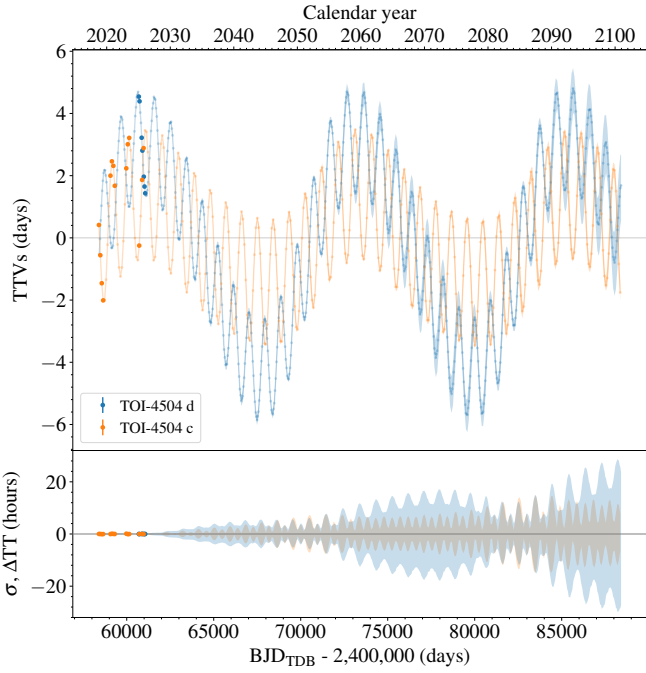


**Fig. 7.** Same as Fig. 2, but up to the year 2100. With linear ephemeris:  $2458422.235250 + 41.2502075 \times \text{epoch (BJD}_{\text{TDB}})$ ,  $2458400.988431 + 82.7810389 \times \text{epoch (BJD}_{\text{TDB}})$  for planet b and c, respectively.

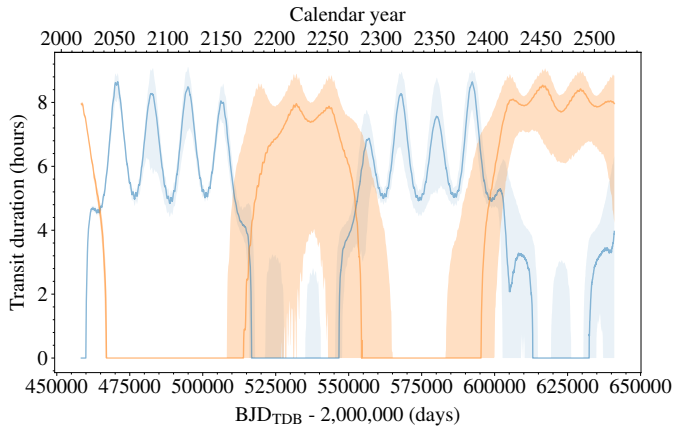


**Fig. 8.** Same as Fig. 3, but for the following 500 years. The oscillation on top of the 250 year nodal precession cycle corresponds to the periastron precession at the superperiod (33 years).

et al. 2005, 2010; Correia et al. 2010; Millholland et al. 2018; Moutou et al. 2023). Lee & Peale (2002) recognized that the unusual alignment of the orbits of the giant pair c and b and their significant eccentricities could not be understood with simple linear theory. Here we use a new formulation of the problem (Mardling *in prep*; hereafter M1 and summarized in Appendix B) to highlight and understand some of the striking similarities between the giant pairs orbiting TOI-4505 and GJ 876, and discuss the implications for the formation of resonant giants.

**Table 2.** Transit times of the observations.

Epoch	Posterior median and 68.3% CI [BJD <sub>TDB</sub> ]	TESS Sector / Instrument
<b>Planet d</b>		
0	2460695.5378 ± 0.0035	88
1	2460736.6378 <sup>+0.0034</sup> <sub>-0.0033</sub>	89
4	2460859.2170 <sup>+0.0034</sup> <sub>-0.0035</sub>	94
5	2460900.0533 ± 0.0031	95
7	2460981.7147 <sup>+0.0035</sup> <sub>-0.0036</sub>	97
8	2461022.6487 ± 0.0034	98
9	2461063.6822 <sup>+0.0014</sup> <sub>-0.0013</sub>	ECAM
<b>Planet c</b>		
0	2458401.4028 ± 0.0030	3
1	2458483.2113 ± 0.0022	6
2	2458565.0920 <sup>+0.0023</sup> <sub>-0.0024</sub>	9
3	2458647.3219 <sup>+0.0027</sup> <sub>-0.0028</sub>	12
8	2459065.2363 ± 0.0022	28
9	2459148.4782 <sup>+0.0024</sup> <sub>-0.0025</sub>	31
10	2459231.1147 ± 0.0021	34
11	2459313.2536 ± 0.0020	37
19	2459976.0635 <sup>+0.0049</sup> <sub>-0.0050</sub>	61
20	2460059.6186 ± 0.0022	64
21	2460142.6049 ± 0.0028	67
28	2460718.6090 <sup>+0.0052</sup> <sub>-0.0051</sub>	89
30	2460886.2837 ± 0.0043	95
31	2460970.0864 <sup>+0.0077</sup> <sub>-0.0075</sub>	97
32	†	ECAM

**Notes.** † Only the egress was observed, and the planet exhibits transit-duration variations, so an independent transit time cannot be derived.

To avoid confusion regarding the order of the orbital periods of the pair TOI-4505d and TOI-4505c, and similarly of the pair GJ 876c and GJ 876b, in this section we will use the subscripts “i” and “o” to indicate “inner” and “outer” for the two giant planets in 2:1 resonance.

The dynamical state of a multiplanet system is of particular interest for the constraints it places on the system’s formation and subsequent evolution. In particular, the period ratios, eccentricities and orbital orientations provide evidence for planet-disk interaction when they are close to one of the relaxed states predicted by migration theory and simulations; if they are not, further insight is required. Planet-planet scattering is often invoked, either at the time of formation (eg. [Rasio & Ford 1996](#)) or as a consequence of long-term instability (eg. [Kokubo et al. 2025](#); [Izidoro et al. 2017](#)). Evidence for the latter is arriving with the characterization of very young systems ([Dai et al. 2023, 2024](#)).

With an increasing number of transiting systems being accurately characterized using photodynamical analysis, it is becoming clear that the architecture of low-mass planetary systems often seem to be inconsistent with simple migration theory. Especially curious are systems for which the forced component of the eccentricities are damped to their non-zero stationary values as expected, while the free components are not; these states are called “supercycles” in M1 (see [Appendix B](#) for new definitions of forced and free eccentricity which are valid for all configurations close to a first-order commensurability, and the various supercycle systems listed there under point (x)). In this respect it will be particularly interesting to see if the free components of young systems follow suit once they are accurately characterized. In contrast, the giant pairs in TOI-4504 and GJ 876 *do* seem to conform with formation theory with little subsequent evolution, a remarkable fact given their estimated ages of  $10.0^{+2.9}_{-3.6}$  Gyr and 0.1-5 Gyr respectively ([Vítková et al. 2025](#); [Correia et al. 2010](#)).

We begin with an overview of the relaxation process according to simple migration theory ([Papaloizou & Larwood 2000](#); [Goldreich & Schlichting 2014](#)), using the first-order (in eccentricity) formulation of M1 to describe the possible final states ([Appendix B](#)). Note that while first-order Hamiltonian formulations are available (e.g., [Batygin 2015](#); [Nesvorný & Vokrouhlický 2016](#); [Petit et al. 2017](#)), M1 uses a general dynamical systems approach which provides physical intuition and remains close to the familiar orbital elements.

While the process of migration tends to damp a single planet’s orbital eccentricity completely (at least when the disk is not eccentric, [Kley & Nelson 2012](#)), for two planets converging towards a low-order commensurability, an eventual balance between the difference in disk torques and the planet-planet torque leaves the pair with a constant period ratio and constant non-zero eccentricities, or finds its equilibrium in a limit-cycle state in which these quantities librate around a fixed-point (“overstable libration”, [Goldreich & Schlichting 2014](#)). Moreover, after such a state is reached, it persists as the planets continue to migrate until the disk disappears. This assumes the latter occurs before the system reaches the disk edge as seems to be the case for the giant pairs in TOI-4504 and GJ 876; here material between the planets is likely to have been completely absent by the time resonance capture occurred due to gap clearing, with convergent migration being outward for the inner planet and inward for the outer planet ([Bryden et al. 2000](#); [Kley 2000](#)).

If the additional acceleration of the planets produced by the disk can be characterised by a tangential and radial component

such that its form is

$$\mathbf{a} = -\tau_a^{-1}\dot{\mathbf{r}} - 2\tau_e^{-1}(\dot{\mathbf{r}} \cdot \hat{\mathbf{r}})\hat{\mathbf{r}}, \quad (1)$$

where  $\mathbf{r}$  is the position of the planet relative to the star (or to the centre of mass of the star-planet system interior to the orbit) and  $\tau_a$  and  $\tau_e$  are the migration and eccentricity damping timescales ([Papaloizou & Larwood 2000](#)), then the equilibrium eccentricities will be  $\sim \sqrt{\tau_e/\tau_a}$  ([Goldreich & Schlichting 2014](#)) and the distance to exact commensurability  $\sim (m_{co}/m_*)\sqrt{\tau_a/\tau_e}$  (M1), where  $m_{co}$  is the mass of the companion planet (see [Eq. \(B.7\)](#)). Therefore the closer the two damping timescales are, the higher the eccentricities and the smaller the distance to exact commensurability. [Papaloizou & Terquem \(2010\)](#) adopt a value of  $\tau_a/\tau_e \simeq 400$  for Type I migration which leads to eccentricities of  $\sim 0.05$  (more like 0.02 when appropriate factors are included; see [Eq. \(24\) of Goldreich & Schlichting 2014](#)). While such eccentricities are typical in chains of low-mass planets, they are considerably smaller than those of the inner giants of TOI-4504 and GJ 876 which are 0.29 and 0.26 respectively. Moreover, both are close to or at their equilibrium values (see below), suggesting that  $\tau_a$  and  $\tau_e$  have similar values for Type II migration of pairs of giants (at least for these two systems; see [Kley et al. 2005](#) for a discussion of migration scenarios for GJ 876).

In addition to non-zero relaxed eccentricities, the resonance-capture process results in orbital anti-alignment when the equilibrium eccentricities are small, as is easily demonstrated using first-order theory (see [Appendix B](#) and [Eq. \(B.7\)](#)). The theory also shows that the associated eccentricity vectors (expressed as complex numbers and involving the mean longitudes) can be decomposed into “forced” (or *resonant*) and “free” (or *secular*) components ([Appendix B](#), point (viii)),<sup>3</sup> and that while the forced eccentricities relax to their equilibrium values as discussed above, the free components relax to zero (M1).

Noting that our photodynamical analysis yields small uncertainties for the eccentricities ([Table 1](#)), [Table 3](#) lists various relevant dynamical parameters for the giant pairs in TOI-4504 and GJ 876, while [Figs. 9 and 10](#) compare their evolution over 20 years. The dynamical states of the two systems are remarkably similar, with each having:

- (i) Inner eccentricities  $\sim 0.25 - 0.3$ ;
- (ii) Similar inner planet-to-star mass ratios (in spite of significantly different stellar masses);
- (iii) Both resonance angles (and hence the difference in the longitudes of periastron) librating around zero;
- (iv) A phase space position deep in the 2:1 resonance and close to the fully-relaxed state ([Fig. 10](#));

<sup>3</sup> Note that the definitions of forced and free eccentricity given in M1 and [Appendix B](#) are different to those in [Lithwick et al. \(2012\)](#), the latter formulated for non-librating systems (often referred to as being “outside the resonance”, although the phase space need not be resonant for a system to be librating). In particular, for M1 the forced component is associated with energy and angular momentum exchange between the orbits which involves variations of both the eccentricities and semi-major axes with associated resonant period  $P_R$ , while the free part is constant at first-order in eccentricity (see [Sect. B.2](#) for the meaning of “free” in [Lithwick et al. 2012](#)). A consequence of this is that TTVs only become sensitive to the free components at second order so that for systems with small eccentricities there is considerable degeneracy in their photodynamical modelling (a good example of this phenomenon is K2-19, [Almenara et al. 2025b](#)). That the eccentricities of the giant pair in TOI-4504 can be measured from the TTVs with such small uncertainties is a direct consequence of the fact that the free eccentricities vary due to nonlinear interaction between the forced and free modes.

**Table 3.** Dynamical parameters of TOI-4504 and GJ 876.

System	$\bar{P}_o/\bar{P}_i$	$e_i, e_i^{(+)}, e_i^{(\text{free})}$	$e_o, e_o^{(+)}, e_o^{(\text{free})}$	$\langle\omega_i - \omega_o\rangle, (\langle\phi_1\rangle, \langle\phi_2\rangle)$	$m_*/M_\odot$	$m_i/m_*, m_o/m_*, m_o/m_i$	$R$	$P_S, P_R$ (yr)
TOI-4504	2.006 [2.017]	0.293, [0.243], [0.038]	0.050, [0.054], [0.106]	0, (0,0)	0.88	0.002, 0.003, 1.3	172 [50]	33.4, 2.5 [13.6], [1.8]
GJ 876	2.0174 [2.047]	0.257, [0.246], [0.019]	0.033, [0.022], [0.053]	0, (0,0)	0.33	0.002, 0.008, 3.2	21 [12]	7.3, 1.5 [3.8], [1.0]

**Notes.** First-order theory values are shown in square brackets, with  $e_i^{(+)}/e_o^{(+)} = (m_o/m_i)\alpha^{-1/2}|v_1|/v_2 = 3.50(m_o/m_i)$  and  $e_i^{(\text{free})}/e_o^{(\text{free})} = v_2/|v_1| = 0.36$  for 2:1. Notice that  $e_i \simeq e_i^{(\text{free})} + e_i^{(+)}$  and  $e_o \simeq e_o^{(\text{free})} - e_o^{(+)}$  (see (b) panels of Fig. 9).

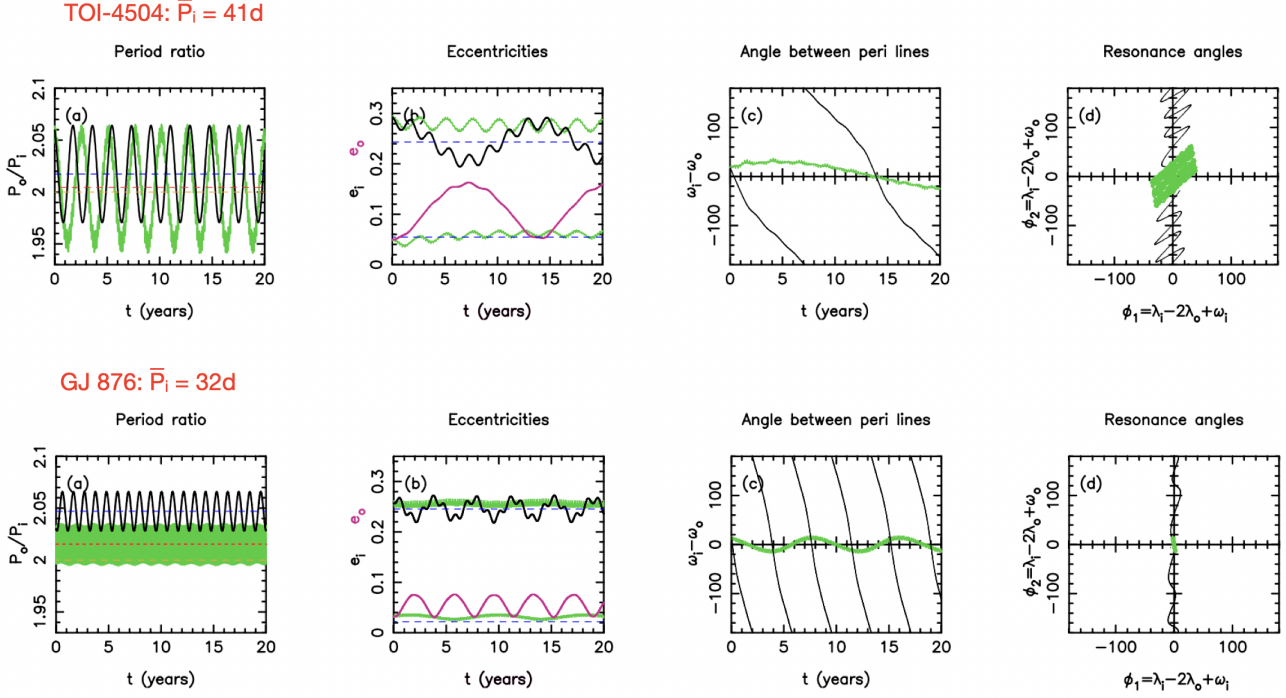


**Fig. 9.** Dynamical evolution of TOI-4504 and GJ 876. Green curves are  $N$ -body integrations with initial conditions from the photodynamical MAP solution for TOI-4504, and the elements at epoch for the best-fit (radial velocity) coplanar four-planet fit of Millholland et al. (2018) for GJ 876. The black and pink curves show first-order theory solutions to the system (Eq. (B.10)), with  $P_o/P_i = (n+1)/n + (1+\theta')\Delta\sigma$ ,  $e_i = [z_1 z_1^*]^{1/2}$  with  $z_1$  from Eq. (B.22) and similarly for  $e_o$  via  $z_2$ , the resonance angles from the phases of  $z_1$  and  $z_2$  (see Eq. (B.1)), and  $\varpi_i - \varpi_o = \phi_1 - \phi_2$ . The blue-dashed lines correspond to first-order theory equilibria, the orange-dashed line in (a) to exact commensurability, and the red-dashed line in (a) to the average value of the true period ratio. Notice that the true  $\phi_1$ ,  $\phi_2$  and  $\varpi_i - \varpi_o$  all librate around zero, consistent with linear theory for  $\phi_1$  because  $e_i^{(+)} > e_i^{(\text{free})}$ , but not for  $\phi_2$  for which theory predicts circulation because  $e_o^{(+)} < e_o^{(\text{free})}$ , and therefore circulation of  $\varpi_i - \varpi_o$  (Appendix B). See text for discussion regarding the current evolution of the eccentricities which reveals that both systems are close to the fully relaxed state.

(v) Significantly non-zero *relaxed* free eccentricity (Fig. 10); this aspect is especially interesting for the discussion below and is the reason it is possible to measure the eccentricities and apsidal angles with such low uncertainties.

Figure 9 compares the predictions of first-order theory (black and pink curves) with  $N$ -body integrations (green curves). Two periods are clearly evident. The shorter resonant period,  $P_R$ , governs the variation of the period ratio which theory underestimates by a factor of 1.4-1.5, while the difference in the apsidal angles is dominated by the superperiod,  $P_S$ , the true value of which is underestimated by a factor of 2-2.5. Both periods are obvious in the theoretical variation of the eccentricities, with large amplitude variations associated with the superperiod, while the true variation is almost exclusively governed by the resonant frequency for TOI-4504 (with amplitude well-predicted by theory). The resonant frequency is almost absent from the true eccentric-

ities of GJ 876. For both systems the true eccentricities are such that their average values are

$$\langle e_i^N \rangle \simeq e_i^{(\text{free})} + e_i^{(+)} \quad \text{and} \quad \langle e_o^N \rangle \simeq e_o^{(\text{free})} - e_o^{(+)}, \quad (2)$$

where the superscript  $N$  denotes  $N$ -body,  $e_i^{(+)}$  and  $e_o^{(+)}$  are the inner and outer primary equilibrium eccentricities predicted by linear theory (blue dashed lines), and  $e_i^{(\text{free})}$  and  $e_o^{(\text{free})}$  are the corresponding free eccentricities. That  $\langle e_i^N \rangle$  and  $\langle e_o^N \rangle$  can be expressed in this way is explained below.

While the free eccentricities are constant at linear order (as are their associated apsidal angles), and moreover are zero in the fully relaxed state, at higher order this is no longer true. In fact given the high eccentricities of TOI-4504 and GJ 876, themselves a result of the close proximity of the average period ratio to exact commensurability, nonlinear interaction between the

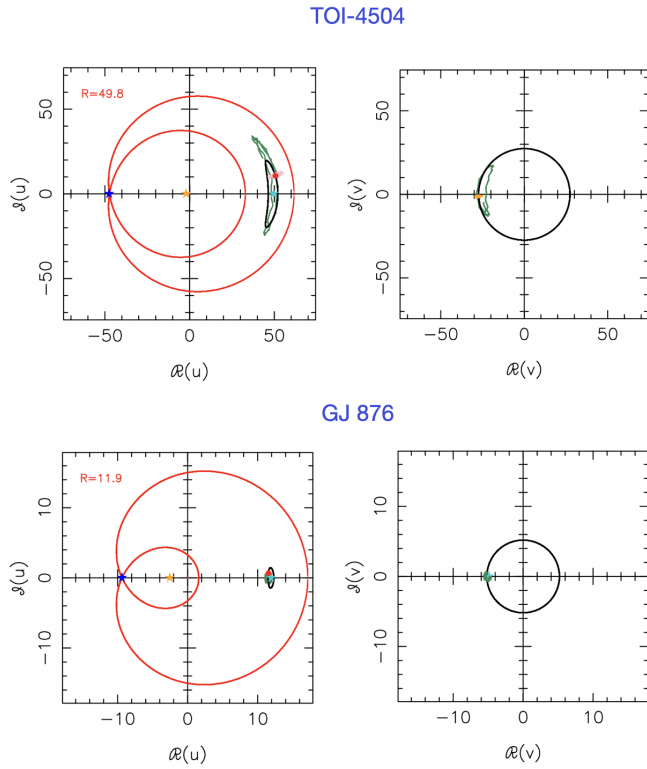


**Fig. 10.** Phase plots for TOI-4504 and GJ 876, with initial conditions for GJ 876 from Millholland et al. (2018). The axes are the real and imaginary parts of  $u$  and  $v$ , defined in Eqs. (B.8) and (B.9). Green curves are  $N$ -body solutions while black curves are from first-order theory. Note that for both systems  $|v|$  is a significant fraction of  $R$ , indicating the strength of interaction between the resonant and secular modes. Both systems are close to their primary fixed points and are likely to be fully relaxed in limit-cycle states; see text for detailed discussion. Notice different scales for TOI-4504 and GJ 876.

resonant and secular modes is significant enough to flip the equilibrium value of the resonance angle  $\phi_2$  from  $\pi$  to zero (with  $\phi_1$  remaining at zero), so that the difference in apsidal angles librates around zero rather than  $\pi$  (panels (c) and (d) of Fig. 9), and to make the relaxed value of the free eccentricity non-zero and the associated free apsidal angles (which are the same for both planets) a function of time. *This latter fact makes the free eccentricity visible to the TTVs, which in turn allows for precise determination of the full eccentricity vectors as long as the observing baseline covers enough of the superperiod.*

Moreover, since the values of the phase-space quantities  $u$  and  $v$  (defined in Eqs. (B.8) and (B.9) and plotted in Fig. 10) are non-zero and almost constant for TOI-4504 and GJ 876, we have from Eqs. (B.27), (B.28) and (B.29) that

$$\langle \dot{\omega}^{(\text{free})} \rangle = \langle \dot{\omega}^{(\text{forced})} \rangle = -\langle \dot{\lambda}_n \rangle \equiv \nu_S = 2\pi/P_S, \quad (3)$$

where  $-\lambda_n$  is the longitude of conjunctions defined in Eq. (B.3). Thus the average rates of advance of the forced and free apsidal lines follow the line of conjunctions and are equal to the superfrequency, which by Eqs. (B.1), (B.22) and (B.23) implies that the apsidal lines themselves follow the line of conjunctions, that is,

$$\langle \dot{\omega}_i \rangle = \langle \dot{\omega}_o \rangle = \nu_S. \quad (4)$$

Note that if TOI-4504 had been precisely at the primary fixed point (the aqua stars in Fig. 10), only the superperiod

$P_S \approx 33.4$  yr would be present in the TTV signal; that it is not means that the much shorter resonant period  $P_R = 2.5$  yr is also present, allowing for full characterization of the system on a 7 year baseline.

The expressions (2) are consistent with the M1 definition of a supercycle state for which the forced components of the eccentricity variables  $z_1$  and  $z_2$  reside at a fixed point and the free components are non-zero. Such a state implies that at the time of resonance capture the damping timescale of the forced component was shorter than that of the free component (see point (x) in Appendix B which includes a list of observed systems close to the supercycle state). For our purposes here, the linear theory predicts that when  $e_1^{(\text{free})}/e_1^{(+)} < 1$  and  $e_0^{(\text{free})}/e_0^{(+)} > 1$ , as is the case for both TOI-4504 and GJ 876, the maxima and minima of the variation of the eccentricities are such that

$$e_i^{(\text{max,min})} = e_i^{(+)} \pm e_i^{(\text{free})} \quad \text{and} \quad e_o^{(\text{max,min})} = e_o^{(\text{free})} \pm e_o^{(+)}. \quad (5)$$

But in the linear theory, non-zero free eccentricity implies that the system is not fully relaxed, while at higher orders the relaxed values of the free eccentricities are not zero. Although such relaxed values tend to be much smaller than any residual true free eccentricity, for TOI-4504 and GJ 876 they are significant, especially for the outer planets (Table 3). The black (first-order theory) and green ( $N$ -body) curves in the top right-hand panel of Fig. 10 shows the evolution of the real and imaginary components of the secular phase-space quantity  $v$  (Eq. (B.9)) for TOI-4504, whose magnitude is proportional to the free eccentricities (Eq. (B.25)). Also shown in orange are 7000 posterior samples for this quantity, revealing that  $v$  is tightly constrained. In the linear theory the magnitude of  $v$  (the radius of the black circle) is constant, while its completely relaxed value is zero. In contrast the green curve shows the actual evolution of this quantity, with libration around a negative real value, the latter being the true equilibrium value of  $v$  (and hence giving the true free eccentricities via Eq. (B.25)). *The fact that the  $N$ -body MAP solution and posterior values are near this value tells us that the TOI-4504 system is close to or actually fully relaxed (if in a limit-cycle state; see point (ix)(B) in Appendix B), implying very little evolution since formation.* Moreover, the fact that  $v$  remains close to its negative equilibrium value over a libration cycle<sup>4</sup> explains why the true amplitudes of the super components of the eccentricities are small (green curves in panel (b) of Fig. 9), and why the average values of the true eccentricities are given by Eq. (2).

The corresponding black and green curves in the top left-hand panel of Fig. 10 shows the evolution of the real and imaginary components of the resonant phase-space quantity  $u$  (Eq. (B.8)) for TOI-4504, together with the separatrix (red curve), the primary fixed point (aqua star), the hyperbolic fixed point (blue star), and 7000 posterior samples for  $u$  (pink dots), again revealing that this quantity is tightly constrained. The red dot is the MAP value of  $u$ . Just as for  $v$ ,  $u$  remains close to its equilibrium value, however its variation is responsible for TTV detection over the 7 year observing baseline; again had the system been in the stationary state the  $P_R = 2.5$  yr resonant period would not be present in the signal, leaving only the  $P_S = 33$  yr period.

The bottom two panels of Fig. 10 show the same analysis for GJ 876, revealing that it is even closer to its stationary state than TOI-4504.

<sup>4</sup> Since there is nonlinear interference between the  $u$  and  $v$  modes, both the resonant and super frequencies influence their variation; the libration cycle shown here has period  $P_R$ .

Finally, as outlined in the Appendix the linear theory can be used to estimate the resonant and superperiods; these are listed in square brackets in Table 3 for both TOI-4504 and GJ 876. But the true periods are considerably longer, a result of the fact that the average value of the period ratio is closer to exact commensurability than predicted by linear theory. As a consequence, both systems are deeper in the 2:1 resonance than suggested by the already high linear-theory values of the resonance parameter  $R$  of 50 and 12 respectively. Estimates of the true values of  $R$  are given in Table 3, obtained using the true values of  $P_R$  and  $P_S$  in Eq. (B.15) with the ansatz that this relationship is valid generally for systems close to the primary fixed point.

#### 4.3. Summary of impact of nonlinear effects on the TTVs

When the eccentricities of a two-planet system are small and the free eccentricities are non-zero, both the free eccentricities and apsidal angles are constant at first order and slowly varying at higher order (hence the designation “secular”; see Appendix B.1 for a discussion of second-order effects). The TTVs are therefore largely insensitive to this component of the eccentricity vectors in this case, producing extensive degeneracy in the eccentricity and apsidal angle projections of the posterior (see Fig. 6 in Almenara et al. 2025b for an example of this phenomenon).

In contrast, when the eccentricities are significant because of a system’s extreme proximity to exact commensurability, a situation likely to be a result of the similarity of the migration and eccentricity damping timescales during Type-II migration, nonlinear interaction between the resonant and secular modes causes the free apsidal lines to evolve, making the free components visible to the TTVs. As a result the eccentricity-orientation degeneracy is lifted, allowing for accurate determination of these quantities (as long as the observing baseline covers enough of the variation, and the photometric precision is adequate).

We again point the reader to Appendix B which presents a self-contained summary of the new and accessible formalism of M1 for the study of systems near a first-order commensurability, whether they be librating or circulating, resonant or non-resonant. The analysis in turn yields simple expressions for the dominant resonant and super harmonics of the TTVs in all these cases (point (vii) in the summary). Note that if both these harmonics (whose associated frequencies are in general non-commensurate) are present in the signal, there is enough information to determine the planet-to-star mass ratios, independent of any degeneracy in the eccentricities and apsidal angles (again see Almenara et al. 2025b where this is demonstrated).

In addition, new general definitions of forced and free eccentricity are introduced which are valid for both librating and circulating systems, offering particular insight into the relaxed states of TOI-4504 and GJ 876. These are compared to the definitions of Lithwick et al. (2012) which only hold for circulating systems sufficiently far from the libration-circulation boundary.

Finally, Appendix B discusses various possible relaxed states, illustrating these with well-characterized systems including TOI-1408, TOI-216, TOI-7510, K2-19, K2-266, Kepler-18, Kepler-36, Kepler-88, Kepler-9 and the Neptune-Pluto system. Note that the formalism provides a simple way to predict the librating or circulating behaviour of the resonance angles when a system is in the librating state (be it resonant or not).

As noted by Vítková et al. (2025), TOI-4504 will be observed by PLATO (Rauer et al. 2014), whose observations are scheduled to begin in 2027. This will establish it as one of the most precisely characterized planetary systems hosting giants,

especially from the point of view of their resonant dynamical evolution.

*Acknowledgements.* This paper includes data collected by the TESS mission. Funding for the TESS mission is provided by the NASA’s Science Mission Directorate. Resources supporting this work were provided by the NASA High-End Computing (HEC) Program through the NASA Advanced Supercomputing (NAS) Division at Ames Research Center for the production of the SPOC data products. This paper includes data collected by the TESS mission that are publicly available from the Mikulski Archive for Space Telescopes (MAST). This work is based on observations collected with EulerCam mounted on the 1.2 m Swiss Euler telescope at La Silla Observatory, Chile. Simulations in this paper made use of the REBOUND code which can be downloaded freely at <http://github.com/hannorein/rebound>. These simulations have been run on the *Bonsai* cluster kindly provided by the Observatoire de Genève. A.L., J.K. and J.M.A. acknowledges support of the Swiss National Science Foundation under grant number TMSGI2\_211697. M.L. acknowledges support of the Swiss National Science Foundation under grant number PCEFP2\_194576. TF acknowledges funding from the French ANR under contract number ANR24-CE493397 (ORVET), and the French National Research Agency in the framework of the Investissements d’Avenir program (ANR-15-IDEX-02), through the funding of the “Origin of Life” project of the Grenoble–Alpes University. This work has been carried out within the framework of the NCCR PlanetS supported by the Swiss National Science Foundation under grant 51NF40\_205606.

## References

- Agol, E., Steffen, J., Sari, R., & Clarkson, W. 2005, *MNRAS*, 359, 567
- Almenara, J. M., Leleu, A., Guillot, T., et al. 2025a, *A&A*, 704, L16
- Almenara, J. M., Mardling, R., Leleu, A., et al. 2025b, *A&A*, 703, A167
- Astropy Collaboration, Price-Whelan, A. M., Lim, P. L., et al. 2022, *ApJ*, 935, 167
- Batygin, K. 2015, *MNRAS*, 451, 2589
- Borsato, L., Degen, D., Leleu, A., et al. 2024, *A&A*, 689, A52
- Borsato, L., Malavolta, L., Piotto, G., et al. 2019, *MNRAS*, 484, 3233
- Bradley, L. 2023, *astropy/photutils*: 1.8.0
- Brasseur, C. E., Phillip, C., Fleming, S. W., Mullally, S. E., & White, R. L. 2019, *Astrotuc: Tools for creating cutouts of TESS images*, *Astrophysics Source Code Library*, record ascl:1905.007
- Broeg, C., Fernández, M., & Neuhäuser, R. 2005, *Astronomische Nachrichten*, 326, 134
- Bryden, G., Różycka, M., Lin, D. N. C., & Bodenheimer, P. 2000, *ApJ*, 540, 1091
- Caldwell, D. A., Tenenbaum, P., Twicken, J. D., et al. 2020, *Research Notes of the American Astronomical Society*, 4, 201
- Carter, J. A., Fabrycky, D. C., Ragozzine, D., et al. 2011, *Science*, 331, 562
- Cochran, W. D., Fabrycky, D. C., Torres, G., et al. 2011, *ApJS*, 197, 7
- Correia, A. C. M., Couetdic, J., Laskar, J., et al. 2010, *A&A*, 511, A21
- Dai, F., Goldberg, M., Batygin, K., et al. 2024, *AJ*, 168, 239
- Dai, F., Masuda, K., Beard, C., et al. 2023, *AJ*, 165, 33
- Deck, K. M., Agol, E., Holman, M. J., & Nesvorný, D. 2014, *ApJ*, 787, 132
- Delfosse, X., Forveille, T., Mayor, M., et al. 1998, *A&A*, 338, L67
- Demory, B.-O. & Seager, S. 2011, *ApJS*, 197, 12
- Espinoza, N., Kossakowski, D., & Brahm, R. 2019, *MNRAS*, 490, 2262
- Fausnaugh, M. M., Burke, C. J., Ricker, G. R., & Vanderspek, R. 2020, *Research Notes of the American Astronomical Society*, 4, 251
- Foreman-Mackey, D. 2016, *The Journal of Open Source Software*, 1, 24
- Foreman-Mackey, D., Agol, E., Ambikasaran, S., & Angus, R. 2017, *AJ*, 154, 220
- Foreman-Mackey, D., Hogg, D. W., Lang, D., & Goodman, J. 2013, *PASP*, 125, 306
- Fortney, J. J., Marley, M. S., & Barnes, J. W. 2007, *ApJ*, 659, 1661
- Garcia, L. J., Timmermans, M., Pozuelos, F. J., et al. 2022, *MNRAS*, 509, 4817
- Goldreich, P. & Schlichting, H. E. 2014, *AJ*, 147, 32
- Goodman, J. & Weare, J. 2010, *Communications in applied mathematics and computational science*, 5, 65
- Guillot, T. 2005, *Annual Review of Earth and Planetary Sciences*, 33, 493
- Hojjatpanah, S., Oshagh, M., Figueira, P., et al. 2020, *A&A*, 639, A35
- Holman, M. J. & Murray, N. W. 2005, *Science*, 307, 1288
- Householder, A. & Weiss, L. 2022, *arXiv e-prints*, arXiv:2212.06966
- Irwin, J. B. 1952, *ApJ*, 116, 211
- Izidoro, A., Ogihara, M., Raymond, S. N., et al. 2017, *MNRAS*, 470, 1750
- Jenkins, J. M., Twicken, J. D., McCauliff, S., et al. 2016, in *Society of Photo-Optical Instrumentation Engineers (SPIE) Conference Series*, Vol. 9913, Software and Cyberinfrastructure for Astronomy IV, 99133E
- Jiang, I.-G., Yeh, L.-C., Edwards, B., et al. 2025, *AJ*, 169, 243
- Kafer, A., Stahl, O., Tubbesing, S., et al. 1999, *The Messenger*, 95, 8
- Kipping, D. M. 2010, *MNRAS*, 408, 1758

- Kipping, D. M. 2013, *MNRAS*, 435, 2152
- Kley, W. 2000, *MNRAS*, 313, L47
- Kley, W., Lee, M. H., Murray, N., & Peale, S. J. 2005, *A&A*, 437, 727
- Kley, W. & Nelson, R. P. 2012, *ARA&A*, 50, 211
- Kokubo, E., Hoshino, H., Matsumoto, Y., & Sari, R. 2025, *ApJ*, 991, L49
- Korth, J., Chaturvedi, P., Parviainen, H., et al. 2024, *ApJ*, 971, L28
- Kreidberg, L. 2015, *PASP*, 127, 1161
- Lange, J. U. 2023, *MNRAS*, 525, 3181
- Lee, M. H. & Peale, S. J. 2002, *ApJ*, 567, 596
- Lendl, M. 2014, PhD thesis, University of Geneva, Switzerland
- Lendl, M., Anderson, D. R., Collier-Cameron, A., et al. 2012, *A&A*, 544, A72
- Lightkurve Collaboration, Cardoso, J. V. d. M., Hedges, C., et al. 2018, *Lightkurve: Kepler and TESS time series analysis in Python*, *Astrophysics Source Code Library*
- Lithwick, Y., Xie, J., & Wu, Y. 2012, *ApJ*, 761, 122
- Lodders, K. & Fegley, B. 2002, *Icarus*, 155, 393
- Malhotra, R. 1993, *Nature*, 365, 819
- Marcy, G. W., Butler, R. P., Fischer, D., et al. 2001, *ApJ*, 556, 296
- Marcy, G. W., Butler, R. P., Vogt, S. S., Fischer, D., & Lissauer, J. J. 1998, *ApJ*, 505, L147
- McKee, B. J. & Montet, B. T. 2023, *AJ*, 165, 236
- Millholland, S., Laughlin, G., Teske, J., et al. 2018, *AJ*, 155, 106
- Moutou, C., Delfosse, X., Petit, A. C., et al. 2023, *A&A*, 678, A207
- Murray, C. D. & Dermott, S. F. 1999, *Solar System Dynamics*
- Nesvorný, D., Chrenko, O., & Flock, M. 2022, *ApJ*, 925, 38
- Nesvorný, D., Kipping, D., Terrell, D., et al. 2013, *ApJ*, 777, 3
- Nesvorný, D. & Vokrouhlický, D. 2016, *ApJ*, 823, 72
- Papaloizou, J. C. B. & Larwood, J. D. 2000, *MNRAS*, 315, 823
- Papaloizou, J. C. B. & Terquem, C. 2010, *MNRAS*, 405, 573
- Petit, A. C., Laskar, J., & Boué, G. 2017, *A&A*, 607, A35
- Rasio, F. A. & Ford, E. B. 1996, *Science*, 274, 954
- Rauer, H., Catala, C., Aerts, C., et al. 2014, *Experimental Astronomy*, 38, 249
- Rein, H. & Liu, S. F. 2012, *A&A*, 537, A128
- Rein, H. & Tamayo, D. 2015, *MNRAS*, 452, 376
- Ricker, G. R., Winn, J. N., Vanderspek, R., et al. 2015, *Journal of Astronomical Telescopes, Instruments, and Systems*, 1, 014003
- Rivera, E. J., Laughlin, G., Butler, R. P., et al. 2010, *ApJ*, 719, 890
- Rivera, E. J., Lissauer, J. J., Butler, R. P., et al. 2005, *ApJ*, 634, 625
- Sessin, W. & Ferraz-Mello, S. 1984, *Celestial Mechanics*, 32, 307
- Sing, D. K., Rustamkulov, Z., Thorngren, D. P., et al. 2024, *Nature*, 630, 831
- Smith, J. C., Stumpe, M. C., Van Cleve, J. E., et al. 2012, *PASP*, 124, 1000
- Smith, P. & Jordan, D. W. Smith, P. 2007, *Nonlinear ordinary differential equations*, fourth edition edn. (Oxford New York: Oxford University Press)
- Speagle, J. S. 2020, *MNRAS*, 493, 3132
- Stumpe, M. C., Smith, J. C., Catanzarite, J. H., et al. 2014, *PASP*, 126, 100
- Stumpe, M. C., Smith, J. C., Van Cleve, J. E., et al. 2012, *PASP*, 124, 985
- Verbiest, G. J. & Rost, M. J. 2015, *Nature Communications*, 6, 6444
- Vissapragada, S., Jontof-Hutter, D., Shporer, A., et al. 2020, *AJ*, 159, 108
- Vítková, M., Brahm, R., Trifonov, T., et al. 2025, *ApJ*, 978, L22
- Welbanks, L., Bell, T. J., Beatty, T. G., et al. 2024, *Nature*, 630, 836

## Appendix A: Parameter space exploration with the partial dataset of Vítková et al. (2025)

We explored the parameter space around the 2:1 resonance using only the transit times of planet c (Table 2) over the same time span available to Vítková et al. (2025), that is, epochs 0 to 21 (partial dataset). We modeled the transit times with the TTVFast code Deck et al. (2014), adopting a time sampling of 0.1 days and the same reference epoch (2 458 400 BJD<sub>TDB</sub>) as Vítková et al. (2025). We considered only planets d and c, assuming coplanar orbits, and explored the parameter space with the nested-sampling NAUTILUS code (Lange 2023). We found a multimodal posterior (see Fig. A.1). All these modes provide an adequate fit to the transit times (see Fig. A.2). The mode shown in purple, compatible<sup>5</sup> with the solution of Vítková et al. (2025), lies outside the resonance, whereas the red and green modes lie inside the resonance. To obtain a ground truth, we repeated this analysis using all available transit times (Table 2), including those of planet d (full dataset), and found a single mode (black in the plots). The green mode encompasses the posterior of the full dataset.

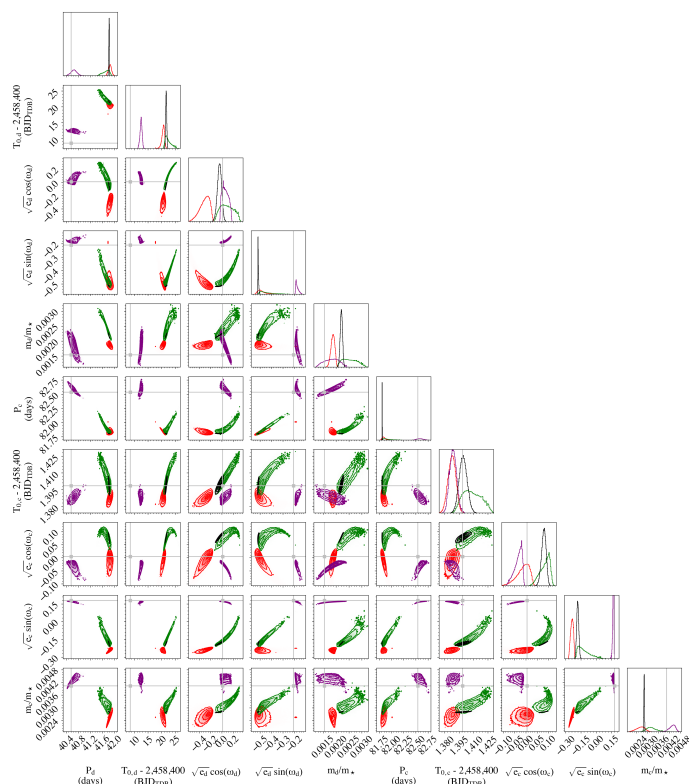


**Fig. A.1.** One- and two-dimensional projections of the posterior sample (Foreman-Mackey 2016) for the jump parameters of the partial-dataset modeling, showing the different modes identified (purple, green, and red). The black posterior corresponds to the full dataset. The solution of Vítková et al. (2025) is indicated in gray. These parameters have a different definition and reference epoch from those used in Sect. 3 and cannot be compared directly.

<sup>5</sup> The match is not exact because of the coplanarity assumption. This difference reflects the additional freedom and the associated complexity introduced when non-coplanar orbits are allowed.

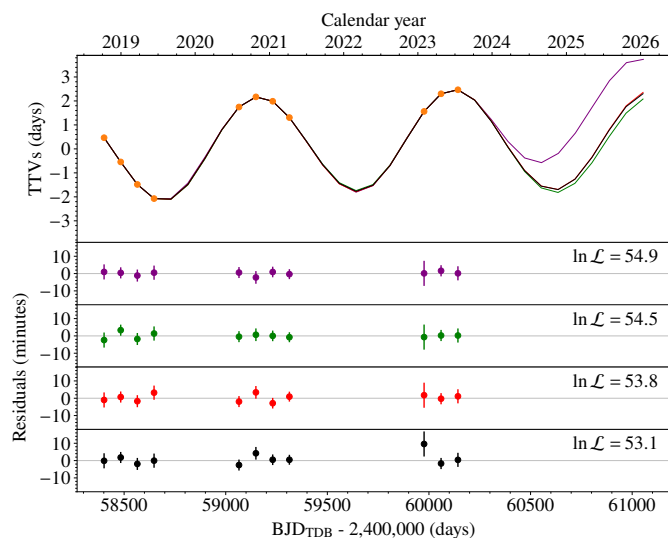


**Fig. A.2.** TTV model and residuals for the maximum-likelihood solution of each mode shown in Fig. A.1 (same color code). The corresponding log-likelihood ( $\ln \mathcal{L}$ ) value is indicated in the residual panel of each model.

## Appendix B: First-order theory

The following provides a summary of the aspects of the first-order theory used in this study (with “first-order” referring to the eccentricities), the full formulation being presented in M1. Using a dynamical systems approach with the fixed points of the phase space serving as reference points, the aim is to keep as close as possible to familiar orbital elements and TTV observables. The formalism is valid for both librating and circulating systems which are close to the period ratio  $P_o/P_i \simeq (n+1)/n$ , where  $n$  is an integer, either of which may reside in a resonant or non-resonant phase space. The concepts introduced are illustrated using various well-characterized systems (highlighted in bold below).

In terms of the usual elements, the eight dimensionless quantities governing a coplanar system close to a first-order commensurability are  $P_o/P_i$ ,  $n\lambda_i - (n+1)\lambda_o$ ,  $e_i$ ,  $e_o$ ,  $\varpi_i$  and  $\varpi_o$ , as well as the planet-to-star mass ratios  $m_i/m_* \equiv \bar{m}_i$  and  $m_o/m_* \equiv \bar{m}_o$ . The elements are first replaced by the two complex quantities

$$z_1 = e_b e^{i\phi_1} \quad \text{and} \quad z_2 = e_c e^{i\phi_2}, \quad (\text{B.1})$$

where

$$\phi_1 = n\lambda_i - (n+1)\lambda_o + \varpi_i \quad \text{and} \quad \phi_2 = n\lambda_i - (n+1)\lambda_o + \varpi_o \quad (\text{B.2})$$

are the resonance angles, and the two real quantities  $\tilde{\theta}$  and  $\dot{\tilde{\theta}}$ , defined such that minus the longitude of conjunctions is

$$\lambda_n(t) \equiv n\lambda_i - (n+1)\lambda_o = \lambda_n(t_{\text{ref}}) + \nu_S(t - t_{\text{ref}}) + \tilde{\theta}(t) - \tilde{\theta}(t_{\text{ref}}). \quad (\text{B.3})$$

Here  $\nu_S = 2\pi/P_S$  is the superfrequency,  $t_{\text{ref}}$  is the reference time, and  $\tilde{\theta}(t)$  captures the exchange of energy and angular momentum between the orbits via the resonant oscillation (with period  $P_R$ ) around the mean increase (or decrease) of  $\lambda_n$ . Note that the definitions (B.1) differ from the complex eccentricities of Lithwick et al. (2012) with the inclusion of the factor  $\lambda_n$  (see Sect. B.2); this allows for the extension of their analysis for circulating systems to resonant and non-resonant librating systems.

As outlined below, the eccentricity variables  $z_1$  and  $z_2$  are then replaced by linear combinations of these two quantities such that one governs the forced (or resonant) component of the interaction and the other governs the free (or secular) component which is not visible to the TTVs at first order. Steps in the M1 formulation are as follows:

(i) *Reduced disturbing function.*

The coplanar disturbing function expanded to first-order in eccentricity and reduced to the two slowly-varying first-order resonant harmonics is

$$\begin{aligned} \mathcal{R} &= m_o a_o^2 \nu_o^2 [v_1(\alpha) e_i \cos \phi_1 + v_2(\alpha) e_o \cos \phi_2] \\ &= \frac{1}{2} m_o a_o^2 \nu_o^2 [v_1 z_1 + v_2 z_2] + CC, \end{aligned} \quad (\text{B.4})$$

where  $CC$  denotes the complex conjugate of the preceding expression,  $\nu_o$  is the outer mean motion,  $\alpha = a_i/a_o \simeq [(n+1)/n]^{-2/3}$  is the ratio of semimajor axes at exact commensurability, and  $v_1(\alpha) < 0$  and  $v_2(\alpha) > 0$  are constants related to Laplace coefficients such that  $v_1 = -1.190$  with  $v_2 = 0.428$  for the 2:1 commensurability. Importantly for the following analysis, notice the linear combination  $v_1 z_1 + v_2 z_2$  in (B.4).

(ii) *Evolution equations.*

From Lagrange’s planetary equations and (B.4), the rates of change of  $z_1$  and  $z_2$  are

$$\dot{z}_1 = i\bar{v}_i \bar{m}_o \alpha v_1 + i(\nu_S + \dot{\tilde{\theta}}) z_1 \quad \text{and} \quad \dot{z}_2 = i\bar{v}_o \bar{m}_i v_2 + i(\nu_S + \dot{\tilde{\theta}}) z_2, \quad (\text{B.5})$$

where  $\bar{v}_i$  and  $\bar{v}_o$  are the “mean-mean motions”. Note that the nonlinear terms  $i(\nu_S + \dot{\tilde{\theta}}) z_1$  and  $i(\nu_S + \dot{\tilde{\theta}}) z_2$  extend the formulation of Lithwick et al. (2012) to all systems close to a first-order commensurability, be they librating or circulating, resonant or non-resonant. The equilibrium values of  $z_1$  and  $z_2$  corresponding to  $\dot{\tilde{\theta}} = 0$  (their primary fixed-point values) are then

$$z_1^{(+)} = -\frac{\bar{m}_o \alpha^{-1/2} v_1}{n\Delta\sigma} \quad \text{and} \quad z_2^{(+)} = -\frac{\bar{m}_i v_2}{n\Delta\sigma}, \quad (\text{B.6})$$

so that the fixed-point eccentricities and resonance angles are

$$e_i^{(+)} = \frac{\bar{m}_o \alpha^{-1/2} |v_1|}{n\Delta\sigma}, \quad e_o^{(+)} = \frac{\bar{m}_i v_2}{n\Delta\sigma}, \quad \phi_1^{(+)} = 0 \quad \text{and} \quad \phi_2^{(+)} = \pi. \quad (\text{B.7})$$

Here  $\Delta\sigma$  is the distance of the primary fixed point to exact commensurability and is such that the superfrequency at the primary fixed point is  $\nu_S^{(+)} = n\nu_o^{(+)} \Delta\sigma$ , where  $\nu_o^{(+)}$  is the outer mean motion at this point. This quantity is determined uniquely from the masses and elements at the reference time (M1), and can be measured if the super and resonant components of the TTV signal can be accurately characterized (Almenara et al. 2025b). Note from (B.2) that to linear order,  $\varpi_i - \varpi_o = \pi$  at the primary fixed point. While this study has no direct use for the equation governing the rate of change of  $\tilde{\theta}$ , we note that  $\dot{\tilde{\theta}}$  is proportional to the linear combination  $v_1 z_1 + v_2 z_2$  (but see (B.10) below).

(iii) *Rotation transformation.*

The reduced disturbing function (B.4) governs the interaction between the orbits to first order in eccentricity via the linear combination  $v_1 z_1 + v_2 z_2$ . It therefore makes sense to define new eccentricity variables such that one is proportional to this quantity, while the other is an independent linear combination of  $z_1$  and  $z_2$  which remains constant during the evolution. Such a transformation was discovered by Sessin & Ferraz-Mello (1984) using a Hamiltonian approach, various versions of which have been employed more recently (e.g., Batygin 2015; Nesvorný & Vokrouhlický 2016; Petit et al. 2017) and each with their own scaling. M1 introduces the following scaling which simplifies the problem considerably. Defining the new variables

$$u = -3 \left( \frac{\sigma}{\Delta\sigma} \right)^2 (\bar{m}_i + \alpha \bar{m}_o) (v_1 z_1 + v_2 z_2) \quad (\text{B.8})$$

and

$$v = -3 \left( \frac{\sigma}{\Delta\sigma} \right)^2 (\bar{m}_i + \alpha \bar{m}_o) (g^{-1} v_2 z_1 - g v_1 z_2) \quad (\text{B.9})$$

with  $\sigma = (n+1)/n$  and  $g = (m_o/m_i)^{1/2} \alpha^{-1/4}$ , the evolution equations take on the especially simple form

$$u' - i(1 + \theta')u = -iR, \quad v' - i(1 + \theta')v = 0 \quad \text{and} \quad \theta'' = -\frac{1}{2i}(u - u^*), \quad (\text{B.10})$$

for which an obvious fixed point is  $(u, v, \theta') = (R, 0, 0)$ ; *this is the primary fixed point*. Here the positive real quantity  $R$  is the *resonance parameter* discussed below and the prime is  $d/dx$ , where  $x = v_S^{(+)}(t - t_{\text{ref}})$  is the scaled “slow” time. The quantity  $\theta$  is related to  $\tilde{\theta}$  such that

$$n\lambda_i - (n+1)\lambda_o = x + \theta = \lambda_n(t_{\text{ref}}) + [1 + \langle \theta' \rangle] x + \tilde{\theta} - \tilde{\theta}(t_{\text{ref}}), \quad (\text{B.11})$$

where  $\langle \theta' \rangle$  is the average value of  $\theta'$  over a complete resonant cycle (which is close to zero when the system is in the librating state and exactly zero at the primary fixed point). Thus in general

$$v_S = [1 + \langle \theta' \rangle] v_S^{(+)}, \quad \Delta S = [1 + \langle \theta' \rangle] \Delta\sigma \quad \text{and} \quad \theta(t_{\text{ref}}) = \lambda_n(t_{\text{ref}}), \quad (\text{B.12})$$

where  $v_S = 2\pi/P_S$  is the superfrequency and  $\Delta S$  is the average distance from exact commensurability.

(iv) *Integrals of the motion.*

The system (B.10) admits the three integrals

$$\frac{1}{2}(1 + \theta')^2 - \frac{1}{2}(u + u^*) = c_E, \quad -2R\theta' + uu^* = c_R = R^2 \quad \text{and} \quad vv^* = c_F, \quad (\text{B.13})$$

where  $c_E$ ,  $c_R$  and  $c_F$  are constants which depend on the initial conditions, with  $c_E$  increasing away from  $c_E^{(\min)} = \frac{1}{2} - R$ , its minimum value at the primary fixed point. The first integral is related to the total energy, while the second and third are such that the quantity  $-2R\theta' + uu^* + vv^*$  is proportional to the angular momentum deficit (AMD, defined relative to the primary fixed point; M1), allowing us the freedom to fix one of  $c_R$  and  $c_F$  (since it is their sum which has physical meaning, and because  $vv^*$  is constant). In fact since the process of capture onto the primary fixed point and any subsequent (adiabatic) evolution away from it tends to preserve the value of the second integral, it makes sense to choose  $c_R = R^2$ , its value at the primary fixed point. Then different level curves in phase-space diagrams such as in Fig. 10 correspond to the same value of  $c_R$  but different values of  $c_E$ .

The first two integrals in (B.13) and the equation for  $\theta''$  in (B.10) can be combined to give a nonlinear differential equation for  $\theta'$ . This can be solved in terms of elliptic functions, whose period is the resonant period  $P_R$  (see Nesvorný & Vokrouhlický (2016) who solve a related equation which arises from an alternative formulation of the problem).

(v) *Resonance parameter  $R$* 

The resonance parameter is the value of  $u$  at the primary fixed point so that from (B.8), (B.6) and (B.7),

$$R = 3 \left( \frac{\sigma}{\Delta\sigma} \right)^2 (\bar{m}_i + \alpha \bar{m}_o) (|v_1| e_i^{(+)} + v_2 e_o^{(+)}). \quad (\text{B.14})$$

As we show in point (vi), its value determines the resonant (or otherwise) nature of the phase space in which a system resides. The masses and the values of the elements at  $t = t_{\text{ref}}$  can be used to determine unique values for  $\Delta\sigma$  and  $R$  as well as  $\theta'(t_{\text{ref}})$ , independent of whether the system is in the librating or circulating state. As long as nonlinear effects are unimportant,  $\Delta\sigma$  and  $R$  remain constant as the system evolves.

In addition, linear stability analysis reveals a relationship between  $R$  and the resonant and superperiod such that

$$R = (P_S/P_R)^2 - 1, \quad (\text{B.15})$$

which is valid for systems close to the primary fixed point.

(vi) *The primary, secondary and hyperbolic fixed points.*

As well as the primary fixed point which exists for all values of  $R$ , there are two other fixed points which exist only for  $R \geq 8$  as the following shows. Note that  $v = 0$  for all three. Since  $\theta' \propto u - u^* = 0$  at all fixed points, they must correspond to real values of  $u$ . From the first integral in (B.13) we can write  $\theta' = (u_0^2 - R^2)/2R$  at the fixed points, where  $u_0$  is real. Substituting this into the first equation in (B.10) and putting  $u' = 0$  then gives

$$u_0^3 - R(R - 2)u_0 - 2R^2 = (u_0 - R)(u_0^2 + Ru_0 + 2R) = 0, \quad (\text{B.16})$$

recovering the primary fixed point  $u_0 = u_0^{(+)} = R$  and providing simple expressions for the stable *secondary fixed point*

$$u_0^{(-)} = -\frac{1}{2}R(1 - \sqrt{1 - 8/R}) \quad (\text{B.17})$$

and the unstable *hyperbolic fixed point*

$$u_0^{(h)} = -\frac{1}{2}R(1 + \sqrt{1 - 8/R}), \quad (\text{B.18})$$

both of which are real only when  $R \geq 8$  (note that  $\Delta\sigma$  and hence  $R$  is positive because resonance capture always occurs long of exact commensurability initially). Linear stability analysis confirms the elliptic and hyperbolic nature of  $u_0^{(-)}$  and  $u_0^{(h)}$  respectively. The existence of a hyperbolic fixed point renders the phase space formally resonant; hence a system is resonant if  $R \geq 8$ . The aqua, orange and blue stars in the left-hand panels of Fig. 10 correspond to the primary, secondary and hyperbolic fixed points respectively.

 (vii) *Transit timing variations.*

In general, three distinct harmonics and their overtones and linear combinations<sup>6</sup> contribute to the TTV signal: the super harmonic, the resonant harmonic and the chopping (synodic) harmonic, whose associated periods are (in general) such that  $P_S > P_R > P_{\text{chop}}$ . Note that the planet-to-star masses ratios can be measured independent of any degeneracy in the eccentricities and apsidal angles if at least two of these harmonics are present in the signal (see Almenara et al. 2025b for a first-principles discussion of how this works). The following discussion pertains to the super and resonant harmonics, for which at first order there is no nonlinear interference.

At first order the super component of the TTV signal is due to variation of the quantities  $e_i \cos \varpi_i$  and  $e_o \cos \varpi_o$  for the inner and outer orbits respectively. The signals are anti-phased with corresponding amplitudes

$$A_S^{(i)} = \left(\frac{P_i}{\pi}\right) e_i^{(S)} \quad \text{and} \quad A_S^{(o)} = \left(\frac{P_o}{\pi}\right) e_o^{(S)} \quad (\text{B.19})$$

where  $e_i^{(S)}$  and  $e_o^{(S)}$  are given by (B.7) with  $\Delta\sigma$  replaced by  $|\Delta S|$ , while the period of variation is the superperiod  $P_S$  due to the combined variation of  $e_i$  and  $\cos \varpi_i$  (and similarly for the outer orbit). Note that for systems residing at the primary fixed point at which the eccentricities and orbital periods are constant and  $\varpi_i - \varpi_o = \pi$ ,  $\dot{\varpi}_i = \dot{\varpi}_o = \nu_S$  so that the TTVs are entirely due to apsidal motion. Note also that this component is present in the signal for all configurations.

The resonant component of the TTV signal is due to energy and angular momentum exchange between the orbits (and hence changes in the orbital periods and eccentricities), and manifests itself through the variation of  $\tilde{\theta}(t) \simeq \Theta_R \cos[\nu_R(t - t_{\text{ref}}) + \beta_R]$  with  $\nu_R = 2\pi/P_R$  and  $\beta_R$  the phase at  $t = t_{\text{ref}}$ . The signals are also anti-phased with corresponding amplitudes

$$A_R^{(i)} = \left(\frac{P_i}{2n\pi}\right) \left(\frac{\alpha m_o}{m_i + \alpha m_o}\right) \Theta_R \quad \text{and} \quad A_R^{(o)} = \left(\frac{P_o}{2(n+1)\pi}\right) \left(\frac{m_i}{m_i + \alpha m_o}\right) \Theta_R, \quad (\text{B.20})$$

while the period of variation is the resonant period  $P_R$ . Since  $\Theta_R = 0$  at each of the fixed-point states, the resonant component is completely absent from the TTV signal in such a state. Finally notice that

$$A_S^{(i)}/A_S^{(o)} = e_i^{(S)}/e_o^{(S)} = \alpha(|v_1|/|v_2|)(m_o/m_i) \quad \text{and} \quad A_R^{(i)}/A_R^{(o)} = \alpha(m_o/m_i). \quad (\text{B.21})$$

 (viii) *Forced and free eccentricity.*

The inverse transformation of the system (B.8) and (B.9) provides natural definitions for forced and free eccentricity which are different to those of Lithwick et al. (2012) (see Sect. B.2 for a comparison). In particular the new definitions distinguish between the parts of the inner and outer eccentricity vectors which are forced (and in general vary) due to the presence of the companion, and the parts which are independent of its presence and are therefore constant (at first order). This is achieved by writing

$$\begin{aligned} z_1 &= \left[ e_b^{(+)} u/R \right] + \left[ -g e_c^{(+)} v/R \right] \\ &\equiv z_1^{(\text{forced})} + z_1^{(\text{free})} \end{aligned} \quad (\text{B.22})$$

<sup>6</sup> Note that linear combinations of non-commensurate frequencies appear as a result of *nonlinear mixing* of the harmonics, introducing new frequencies (Verbiest & Rost 2015). This effect becomes measurable in the TTV signal when the super and resonant frequencies are similar, resulting in the secular variation observed in systems such as **Kepler-88** (Nesvorný et al. 2013) and **TOI-1130** (Borsato et al. 2024) (although the effect is not identified by those authors). It is distinct from *beating* which involves the linear superposition of two or more harmonics and results in amplitude modulation (but introduces no new frequencies).

and

$$\begin{aligned} z_2 &= \left[ -e_c^{(+)} u/R \right] + \left[ -g^{-1} e_b^{(+)} v/R \right] \\ &\equiv z_2^{(\text{forced})} + z_2^{(\text{free})}, \end{aligned} \quad (\text{B.23})$$

with the square brackets indicating the definitions and  $z_1$  and  $z_2$  given by (B.1). From the integrals (B.13) the forced eccentricities are then

$$e_i^{(\text{forced})} = \left[ z_1^{(\text{forced})} z_1^{(\text{forced})*} \right]^{1/2} = \sqrt{1 + 2\theta'/R} e_i^{(+)} \quad \text{and} \quad e_o^{(\text{forced})} = \sqrt{1 + 2\theta'/R} e_o^{(+)}, \quad (\text{B.24})$$

with their oscillations *in phase* (for both the librating or circulating states) and entering via the  $\tilde{\theta}'$  component of  $\theta'$ , while the constancy of  $\nu v^*$  results in constant free eccentricities such that

$$e_i^{(\text{free})} = \left[ z_1^{(\text{free})} z_1^{(\text{free})*} \right]^{1/2} = [g |v(t_{\text{ref}})|/R] e_o^{(+)} \quad \text{and} \quad e_o^{(\text{free})} = [g^{-1} |v(t_{\text{ref}})|/R] e_i^{(+)}. \quad (\text{B.25})$$

Defining the associated apsidal angles  $\varpi_i^{(\text{forced})}$  and  $\varpi_i^{(\text{free})}$  such that

$$z_1^{(\text{forced})} = e_i^{(\text{forced})} e^{i[n\lambda_i - (n+1)\lambda_o + \varpi_i^{(\text{forced})}]} \quad \text{and} \quad z_1^{(\text{free})} = e_i^{(\text{free})} e^{i[n\lambda_i - (n+1)\lambda_o + \varpi_i^{(\text{free})}]} \quad (\text{B.26})$$

and similarly for  $\varpi_o^{(\text{forced})}$  and  $\varpi_o^{(\text{free})}$  via  $z_2^{(\text{forced})}$  and  $z_2^{(\text{free})}$ , then writing the plane polar representations of  $u$  and  $v$  as

$$u = |u| e^{i\psi} \quad \text{and} \quad v = |v| e^{i\varphi} \quad (\text{B.27})$$

where

$$\psi = n\lambda_i - (n+1)\lambda_o + \varpi_\psi \quad \text{and} \quad \varphi = n\lambda_i - (n+1)\lambda_o + \varpi_\varphi, \quad (\text{B.28})$$

we have from (B.22) and (B.23) that

$$\varpi_i^{(\text{forced})} = \varpi_\psi = \varpi_o^{(\text{forced})} + \pi \quad \text{and} \quad \varpi_o^{(\text{free})} = \varpi_\varphi(T_0) + \pi = \varpi_i^{(\text{free})} \equiv \varpi^{(\text{free})} = \text{constant}, \quad (\text{B.29})$$

where the constancy of the free apsidal angle can be demonstrated from the analytic solution for  $\nu$  (M1). Thus the forced components of the eccentricity vectors are anti-aligned, while the free components are aligned and stationary (at first order). Moreover we have that

$$e_i^{(\text{forced})}/e_o^{(\text{forced})} = e_i^{(+)} / e_o^{(+)} = \alpha^{-1/2} (m_o/m_i) |v_1|/v_2 \quad \text{and} \quad e_i^{(\text{free})}/e_o^{(\text{free})} = v_2/|v_1|, \quad (\text{B.30})$$

so that perhaps counter-intuitively, the free components, which indicate the degree to which the system is relaxed, are not independent. Note that the ratios  $e_i^{(\text{free})}/e_i^{(\text{forced})}$  and  $e_o^{(\text{free})}/e_o^{(\text{forced})}$  determine the librating and circulating behaviour of the resonance angles (M1; see also the discussion of supercycles below).

(ix) *Relaxed states.*

A fully relaxed nonlinear mechanical system is one for which the rate of change of total energy is zero in the presence of dissipation (Smith & Jordan 2007). This state may be completely stationary, or may be a limit-cycle (the ‘‘overstable librations’’ of Goldreich & Schlichting 2014). For a (Newtonian) migrating planetary system for which only length ratios (and not absolute lengths) govern the dynamics, this is true in the co-moving frame, and requires that accelerations associated with dissipation be of the form (1) (or similar) in order for eccentricity and period-ratio excitation to take place.

In the linear theory, all fully relaxed two-planet systems have zero free eccentricity so that a useful measure of the degree of relaxation is the ratio

$$r_{\text{AMD}} \equiv \nu v^* / (R^2 + \nu v^*) \quad (\text{B.31})$$

(see Eq. (B.13)). Values of  $r_{\text{AMD}}$  are listed below for various well-characterized systems. Relaxed systems are in one of the following states:

(A) The stationary *primary fixed point* at which  $u = R$ ,  $v = 0$ , with the eccentricities and resonance angles given by (B.7), and the distance,  $\Delta S$ , from exact commensurability positive and equal to  $\Delta\sigma$ . This state may be resonant or non-resonant. As discussed above:

★ **GJ 876c,b** is in this state when higher-order effects are taken into account.

(B) The *primary limit cycle* state at which  $|u| = R \sqrt{1 + 2\theta'/R}$ ,  $\theta' \neq 0$ , and  $v = 0$ , with the eccentricities oscillating in phase with period  $P_R$ , the resonance angles  $\phi_1$  and  $\phi_2$  librating in phase with period  $P_R$  around zero and  $\pi$  respectively if the system is in the librating state, and  $\varpi_i - \varpi_o = \pi$  exactly for both librating and circulating systems. The system may be resonant or non-resonant, although simulations which use simple disk models suggest that resonant systems which reach the separatrix during the capture process tend to move on to the next commensurability.<sup>7</sup> Examples near this state include:

<sup>7</sup> **Kepler-9** is a curious counter-example consisting of a pair of  $0.1M_J$  planets (Borsato et al. 2019) in the circulating state just outside the 2:1 separatrix in a severely-resonant phase space (M1). Note that  $\nu \neq 0$  for this system.

- ★ The **non-resonant librating** system **TOI-1408c,b** (Korth et al. 2024) with parameters  $P_o/P_i = 2.04$ ,  $m_s = 1.3M_\odot$ ,  $m_i = 0.02M_J$ ,  $m_o = 1.9M_J$ ,  $R = 3.4$ ,  $e_i = 0.14$ ,  $e_o = 0.002$ ,  $e_i^{(\text{free})} = 0.0008$ ,  $e_o^{(\text{free})} = 0.002$  and  $r_{\text{AMD}} = 0.04$ ;
  - ★ The **resonant librating** system **TOI-216b,c** (Nesvorný et al. 2022) with parameters  $P_o/P_i = 2.02$ ,  $m_s = 0.77M_\odot$ ,  $m_i = 0.06M_J$ ,  $m_o = 0.6M_J$ ,  $R = 21.1$ ,  $e_i = 0.16$ ,  $e_o = 0.005$ ,  $e_i^{(\text{free})} = 0.002$ ,  $e_o^{(\text{free})} = 0.006$  and  $r_{\text{AMD}} = 0.02$ .
  - ★ **TOI-4504d,c** appears to be in a higher-order limit-cycle state, with the  $v$ -component librating around its non-zero equilibrium value rather than fixed at zero. By simulating the capture process for a system with the same masses and with disk acceleration given by (1),<sup>8</sup> we verified that the phase space behaviour seen in Fig. 10 is indeed a limit-cycle state.
- (C) The stationary *secondary fixed point* (which exists only for  $R \geq 8$ ) at which  $u = u_0^{(-)}$ ,  $\Delta S = \Delta\sigma^{(-)} \equiv u_0^{(h)}\Delta\sigma < 0$  (where  $u_0^{(h)}$  is given in terms of  $R$  by (B.18)), the eccentricities are given by (B.7) but with  $\Delta\sigma$  replaced by  $\Delta\sigma^{(-)}$ , and the resonance angles are  $\phi_1 = \pi$  and  $\phi_2 = 0$ . An example which is very close to this state is:
- ★ **Kepler-18c,d** (Cochran et al. 2011) (2:1; **resonant librating**,  $\Delta S = -0.06$ ,  $r_{\text{AMD}} = 5 \times 10^{-5}$ ).
- (D) The *secondary limit-cycle* state is similar to the primary limit-cycle state but with  $|u| = |u_0^{(-)}| \sqrt{1 + 2\theta'/R}$ . An example of a system close to this state is:
- ★ **TOI-7510b,c** (Almenara et al. 2025a) (2:1; **resonant circulating**,  $\Delta S = -0.04$ ,  $r_{\text{AMD}} = 0.06$ ).
- Note that both Kepler-18c,d and TOI-7510b,c participate in near-Laplace-like configurations (4:2:1).
- (x) *Supercycles*.  
Supercycles are completely relaxed in  $u$ -space but not in  $v$ -space, suggesting that the formation damping timescales are different for each mode, and tend to have high values of  $r_{\text{AMD}}$  which distinguishes them from limit cycles for which  $r_{\text{AMD}} = 0$  at first order. As a result the resonant component of the TTVs is completely absent, and since at first order the free eccentricity and apsidal angle are constant, TTVs can only distinguish this state when (higher-order) nonlinear interference between the resonant and secular modes is significant enough to cause the free quantities to vary. The primary and secondary supercycle states each have four distinct sub-states:
- (A) The primary supercycle state is defined by  $u = u_0^{(+)} = R$ ,  $v \neq 0$ , that is, the resonant ( $u$ ) component is identical to the primary fixed point state but the free eccentricity is non-zero. As a result the period ratio is constant (as are the mean motions), while the eccentricities are anti-phased and vary with period  $P_S$ . The average value of the inner eccentricity is  $e_i^{(+)}$  if  $e_i^{(\text{free})} < e_i^{(+)}$  with amplitude  $e_i^{(\text{free})}$  and  $\phi_1$  librating, while the average value is  $e_i^{(\text{free})}$  if  $e_i^{(\text{free})} > e_i^{(+)}$  with amplitude  $e_i^{(+)}$  and  $\phi_1$  circulating. The situation is similar for the outer eccentricity and  $\phi_2$ , resulting in the four possible states ( $l, l$ ), ( $l, c$ ), ( $c, l$ ) and ( $c, c$ ), where  $l$  and  $c$  stand for the libration or circulation of ( $\phi_1, \phi_2$ ). Note that not all four are possible for a given value of  $m_o/m_i$ .  
Using published parameters (or the whole posterior for K2-19), systems which are close to this state include:
- ★ **Kepler-36b,c** (Vissapragada et al. 2020) (7:6,  $R = 2.5$ , **librating non-resonant**, ( $c, c$ ),  $r_{\text{AMD}} = 0.99$ );
  - ★ **K2-19b,c** (Almenara et al. 2025b) (3:2,  $R = 15.5$ , **librating resonant**, ( $l, l$ ), ( $c, l$ ), ( $c, c$ ),  $r_{\text{AMD}} = 0.85$ );
  - ★ **TOI-1130b,c** (Borsato et al. 2024) (2:1,  $R = 0.23$ , **librating non-resonant**, ( $l, c$ ),  $r_{\text{AMD}} = 0.95$ );
  - ★ **The Pluto-Neptune system** (Malhotra 1993; Murray & Dermott 1999) (3:2,  $R = 3481$ , **librating severely resonant**, ( $l, l$ ),  $r_{\text{AMD}} = 0.89$ ).
- (B) The secondary supercycle state is defined by  $u = u_0^{(-)}$ ,  $v \neq 0$ , that is, the resonant component is identical to the secondary fixed point state but the free eccentricity is non-zero. A system which is very close to this state is:
- ★ **K2-266d,e** (Jiang et al. 2025) (4:3;  $\Delta S = -0.007$ ,  $R = 10.5$ , **librating resonant**, ( $c, c$ ),  $r_{\text{AMD}} = 0.83$ ).

## Appendix B.1: Second-order theory

The purpose of the following is to illustrate how nonlinear mixing of the resonant and secular modes is introduced at second order, and omits contributions from the variation of the mean longitude at epoch and the term involving  $\partial\mathcal{R}/\partial\lambda$  in Lagrange's planetary equation for the rate of change of the eccentricity. Note that the latter terms are second-order in  $u$  and  $v$  in (B.33).

To second-order in eccentricity, three additional slowly-varying harmonics involving  $2\phi_1$ ,  $\phi_1 + \phi_2$  and  $2\phi_2$  are introduced and the reduced disturbing function (B.4) becomes

$$\mathcal{R} = \frac{1}{2}m_o a_o^2 v_o^2 [v_1 z_1 + v_2 z_2 + w_1 z_1^2 + 2w_{12} z_1 z_2 + w_2 z_2^2] + CC, \quad (\text{B.32})$$

where  $w_1(\alpha) > 0$ ,  $w_{12}(\alpha) < 0$  and  $w_2(\alpha) > 0$  are constants related to Laplace coefficients such that  $w_1 = 1.696$ ,  $2w_{12} = -4.967$  and  $w_2 = 3.594$  for the 2:1 commensurability. Substituting the inverse rotation transformation (B.22) and (B.23) into the resulting equations for the rates of change of  $z_1$ ,  $z_2$  and  $\theta$  (and scaling the time) then yields evolution equations for  $u$ ,  $v$  and  $\theta'$  such that

$$u' - i(1 + \theta')u - i(D_{11}u^* + D_{12}v^*) = -iR, \quad v' - i(1 + \theta')v - i(D_{12}u^* + D_{22}v^*) = 0, \quad (\text{B.33})$$

and

$$\theta'' = -\frac{1}{2i} \left[ u - (D_{11}u^2 + 2D_{12}uv + D_{22}v^2)/R \right] + CC, \quad (\text{B.34})$$

with integrals

$$\frac{1}{2}(1 + \theta')^2 - \frac{1}{2}(u + u^*) + \frac{1}{4R} \left[ D_{11}(u^2 + u^{*2}) + 2D_{12}(uv + u^*v^*) + D_{22}(v^2 + v^{*2}) \right] = c_E^{(2)} \quad (\text{B.35})$$

<sup>8</sup> We also included a disk edge to ensure convergent migration given the planet-planet mass ratio is only 1.3.

**Table B.1.** Second-order parameters for various systems, with the magnitude of  $D_{12}$  indicative of the strength of the nonlinear interaction

System	$n + 1 : n$	$R$	$\Delta\sigma$	$m_s, m_i, m_o$	$D_{11}$	$D_{12}$	$D_{22}$	$\nu^{(+)}$
TOI-4504d,c	2:1	50	0.02	0.8, 2.0, 2.5	1.1	<b>0.7</b>	0.5	-14.2
GJ 876c,b	2:1	13.6	0.05	0.3, 0.9, 2.8	0.9	<b>0.4</b>	0.2	-2.9
TOI-1130b,c	2:1	0.2	0.05	0.8, 0.06, 1.1	0.1	<b>0.03</b>	0.007	-0.006
TOI-1408c,b	2:1	3.4	0.02	2.3, 0.02, 1.9	0.3	<b>0.03</b>	0.004	-0.09
K2-19b,c	3:2	15.5	0.003	0.9, 0.09, 0.03	0.003	<b>-0.002</b>	0.001	0.03
Neptune-Pluto	3:2	3481	0.0003	1.0, 0.05, $7 \times 10^{-6}$	1.7	<b>0.0002</b>	$-6 \times 10^{-7}$	-0.3

**Notes.**  $R$  and  $\Delta\sigma$  from first-order theory. Mass units: star  $M_\odot$ , planets  $M_J$ .

and

$$-2R\theta' + uu^* + vv^* = c_J, \quad (\text{B.36})$$

where  $c_E^{(2)}$  and  $c_J$  are constants of the motion. Here the terms in blue introduce mixing of the resonant and secular modes, while the  $D_{ij} \propto \Delta\sigma^{-1}$  depend on the  $v$ 's and  $w$ 's as well as the planet-to-star mass ratios and the planet-to-planet mass ratios. For example, in the limit of large  $m_o/m_i$  (and therefore large  $g = \alpha^{-1/4}(m_o/m_i)^{1/2}$ ) as is the case for TOI-1130 and TOI-1408 (see Table B.1), we have

$$\lim_{g^{-1} \rightarrow 0} D_{11} = e_b^{(+)} d_{11}^{(g\uparrow)}, \quad \lim_{g^{-1} \rightarrow 0} D_{12} = g^{-1} e_b^{(+)} d_{12}^{(g\uparrow)} \quad \text{and} \quad \lim_{g^{-1} \rightarrow 0} D_{22} = \mathcal{O}(g^{-2}), \quad (\text{B.37})$$

where  $d_{11}^{(g\uparrow)} = 2w_1/|v_1|$  is 2.85 for 2:1 and 5.27 for 3:2, while  $d_{12}^{(g\uparrow)} = 2(w_{12}/v_1 - v_2 w_1/v_1^2)$  is 3.15 for 2:1 and 0.11 for 3:2. Similarly for small  $m_o/m_i$  (small  $g$ ),

$$\lim_{g \rightarrow 0} D_{11} = e_c^{(+)} d_{11}^{(g\downarrow)}, \quad \lim_{g \rightarrow 0} D_{12} = g e_c^{(+)} d_{12}^{(g\downarrow)} \quad \text{and} \quad \lim_{g \rightarrow 0} D_{22} = \mathcal{O}(g^2), \quad (\text{B.38})$$

where  $d_{11}^{(g\downarrow)} = 2w_2/v_2$  is 16.78 for 2:1 and 6.65 for 3:2, while  $d_{12}^{(g\downarrow)} = 2(w_{12}/v_2 - v_1 w_2/v_2^2)$  is 35.03 for 2:1 and 0.07 for 3:2.

Table B.1 lists values of  $D_{ij}$  for TOI-4504 and GJ 876, as well as the non-resonant librating systems TOI-1130 (Borsato et al. 2024) and TOI-1408 (Korth et al. 2024), both of which are near the 2:1 commensurability and harbour a giant and a Neptune-like planet. In addition to excellent photometric precision, nonlinear mixing allows for the full eccentricities and apsidal angles to be well characterized for each of these systems, thanks especially to the magnitude of  $D_{12}$  (see Eqs. (B.33) to (B.35) and boldface values in Table B.1). In particular, the contribution to  $\theta'$  from the term proportional to  $D_{12}uv$  in (B.34) modifies  $\Theta$  and hence the TTV resonant amplitudes (B.20), distinguishing between systems with different eccentricities and apsidal angles.

In contrast,  $D_{12}$  tends to be small for systems near the  $n + 1 : n$  commensurability for  $n \geq 2$ , as is the case for K2-19 which is also listed in Table B.1. As a result, the posterior projections of the eccentricities and apsidal angles tend to be highly degenerate for such systems (see Fig. 6 of Almenara et al. 2025b for K2-19).

Also listed in Table B.1 are second-order estimates for the fixed-point values of

$$\nu = \nu^{(+)} = -RD_{12}/|D|, \quad (\text{B.39})$$

obtained by putting  $u' = v' = \theta' = 0$  in (B.33). Here  $|D| = (1 + D_{11})(1 + D_{22}) - D_{12}^2$ . These are around half the true values for both TOI-4504 and GJ 876 (see Fig. 10), which we attribute to the neglect of higher-order terms, but are nonetheless several orders of magnitude higher than for the other systems listed.

### Appendix B.2: Forced and free eccentricity in the Lithwick et al. (2012) formulation

Lithwick et al. (2012) (hereafter LXW) introduce the concepts of forced and free eccentricity for near-resonant systems,<sup>9</sup> defining the inner and outer ‘‘complex eccentricities’’ (using our notation as well as  $\zeta_1$  and  $\zeta_2$  for their  $z$  and  $z'$  to avoid confusion) as  $\zeta_1 = e_1 e^{i\varpi_1}$  and  $\zeta_2 = e_o e^{i\varpi_o}$ . Notice these differ from our definitions of  $z_1$  and  $z_2$  in (B.1) which involve the additional factor  $e^{i\lambda_n}$  (note also that their  $\lambda^j = -(j-1)\lambda_j + j\lambda_o$  is our  $-\lambda_n = -n\lambda_1 + (n+1)\lambda_o$ ). The authors then decompose the complex eccentricities into ‘‘forced’’ and ‘‘free’’ components such that

$$\zeta_1 = \zeta_1^{(\text{forced})} + \zeta_1^{(\text{free})} \quad \text{and} \quad \zeta_2 = \zeta_2^{(\text{forced})} + \zeta_2^{(\text{free})}, \quad (\text{B.40})$$

where

$$\zeta_1^{(\text{forced})} = s e_1^{(S)} e^{-i\lambda_n} = -\zeta_2^{(\text{forced})} \quad (\text{B.41})$$

<sup>9</sup> Note that these are distinct from the definition given in Murray & Dermott (1999) for secular systems.

with  $s = \text{sgn}(\Delta S)$ , and  $\zeta_1^{(\text{free})}$  and  $\zeta_2^{(\text{free})}$  are integration constants (which come from integrating their Eq. (A13)), and remark that “the complex free eccentricities precess on a secular timescale” (i.e., on a timescale much longer than the observations). Note that the quantity  $\Delta \equiv \Delta_{\text{LXW}}$  in LXW is such that  $(n+1)\Delta_{\text{LXW}} = n\Delta S$ . Perturbations to the mean longitudes are derived effectively from conservation of angular momentum,<sup>10</sup> after which they arrive at expressions for the inner and outer TTVs

$$TTV_{i,o}^{\text{LXW}} = \left( \frac{P_{i,o}}{2\pi} \right) |E_{i,o}^{\text{LXW}}| \sin[\nu_S(t - t_{\text{ref}}) + \beta_{i,o}], \quad (\text{B.42})$$

where

$$E_i^{\text{LXW}} = e_i^{(S)} \left[ 1 - \frac{3}{2} \frac{1}{|v_1|} \frac{Z_{\text{free}}^*}{\Delta_{\text{LXW}}} \right] \quad \text{and} \quad E_o^{\text{LXW}} = -e_o^{(S)} \left[ 1 - \frac{3}{2} \frac{1}{v_2} \frac{Z_{\text{free}}^*}{\Delta_{\text{LXW}}} \right], \quad (\text{B.43})$$

for which LXW define the complex quantity

$$Z_{\text{free}} = v_1 \zeta_1^{(\text{free})} + v_2 \zeta_2^{(\text{free})}. \quad (\text{B.44})$$

But this is the combination of eccentricities appearing in the disturbing function (B.4) and in the definition of  $u$  (Eq. (B.8)), so the sense of “free” in the M1 and LXW formulations is quite different. Indeed for M1, “free” refers to the part of the signal which is not detectable at first order and which involves the linear combination appearing in (B.9) rather than (B.44), while for LXW this component does indeed affect the signal. In fact LXW make it clear that their formulation is valid only when  $|Z_{\text{free}}/\Delta_{\text{LXW}}|$  is very large or very small. The first limit corresponds to circulating systems far outside the separatrix/libration boundary where  $|u|$  is approximately constant and  $\langle \dot{\sigma}_{\psi} \rangle \ll \nu_S$ , justifying the statement that the complex free eccentricities evolve secularly, while the second limit corresponds to either of the stable fixed points. Moreover, while librating systems and circulating systems close to the libration boundary vary with period  $P_R$ , far from the libration boundary  $P_R \simeq P_S$ , justifying the single harmonic in (B.42) and causing the mass-eccentricity degeneracy inherent in many system which exhibit TTVs.

While the two TTV formulations are identical at the stable fixed points (where  $\Theta_R$  and  $Z_{\text{free}}$  are zero and from (B.24) the forced eccentricities are the same), they can be reconciled for systems far outside the libration boundary if we define

$$Z_{\text{forced}} \equiv \left( v_1 z_1^{(\text{forced})} + v_2 z_2^{(\text{forced})} \right) e^{-i\lambda_n}, \quad (\text{B.45})$$

where  $z_1^{(\text{forced})}$  and  $z_2^{(\text{forced})}$  are given in (B.22) and (B.23) (notice that  $Z_{\text{forced}}$  is independent of  $\lambda_n$ ), take  $Z_{\text{forced}}$  and the mean motions to be constant, and integrate  $\theta'' = \frac{1}{2}i(u - u^*)$  twice (the third equation in (B.10)). The TTV amplitudes are then (B.43) with  $Z_{\text{free}}$  replaced by  $Z_{\text{forced}}$ .

On the other hand, the LXW formulation says nothing about the free component associated with  $\nu$ , whose magnitude is truly constant at first-order in eccentricity, and varies secularly only at second order through nonlinear interference of the resonant and secular modes.

<sup>10</sup> In fact they use two related integrals.